

University of Alberta

INTERNAL WAVE TUNNELLING: LABORATORY EXPERIMENTS

by

Kate D. Gregory

A thesis submitted to the Faculty of Graduate Studies and Research
in partial fulfillment of the requirements for the degree of

Master of Science

in

Applied Mathematics

Department of Mathematical and Statistical Sciences
Department of Earth and Atmospheric Sciences

©Kate D. Gregory
Spring 2010
Edmonton, Alberta

Permission is hereby granted to the University of Alberta Libraries to reproduce single copies of this thesis and to lend or sell such copies for private, scholarly or scientific research purposes only. Where the thesis is converted to, or otherwise made available in digital form, the University of Alberta will advise potential users of the thesis of these terms.

The author reserves all other publication and other rights in association with the copyright in the thesis and, except as herein before provided, neither the thesis nor any substantial portion thereof may be printed or otherwise reproduced in any material form whatsoever without the author's prior written permission.

Examining Committee

Bruce Sutherland, Physics / Earth & Atmospheric Sciences

Bryant Moodie, Mathematical & Statistical Sciences

Gerhard Reuter, Earth & Atmospheric Sciences

Abstract

Heuristics based upon ray theory are often used to predict the propagation of internal gravity waves in non-uniform media. In particular, they predict that waves reflect from weakly stratified regions where the local buoyancy frequency is less than the wave frequency. However, if the layer of weak stratification is sufficiently thin, waves can partially transmit through it in a process called tunnelling. The first laboratory evidence of internal wave tunnelling through a weakly stratified region is analysed using the synthetic schlieren technique and the Hilbert transform is applied to filter the wavefield into upward- and downward-propagating components. Transmission is calculated as the squared ratio of transmitted and incident wave amplitude and using an appropriate superposition of plane waves to reproduce the structure of the incident wave beam, a corresponding weighted sum of transmissions can be used to predict the beam transmission. These transmission predictions are compared with experimental measurements.

Acknowledgements

I have always believed that life is a journey, not a destination, and these last two years have been a journey that has challenged me to grow in more ways than I could have imagined. There have been a lot of people who have helped me get to where I am today, and I hope that the few words I have room to say here effectively convey my heartfelt thanks.

To my parents, Frank and Claudette, and my sister, Pam, for their lifelong support, I could not have hand-picked a better family.

To my supervisor, Bruce, for teaching me the science, and art, of scientific research. I am constantly amazed by his ability to effectively balance the busy life of a professor which I'm sure has something to do with his reminders to "work hard and play hard". As students, we often joke about how Bruce has ruined all future supervisors for us, but in all honesty, he has.

To my committee members for their time and invaluable contributions to the writing of my thesis.

To my colleagues for making this experience unforgettable. Graduate research is rarely done alone and I had the honour of working beside some of the most inspirational people I know. A special thanks to my shared-brain sister, Heather, for reminding me on those difficult days to take care of the self.

And finally, to my husband, Patrick, and stepson, Pierre, for their undying support, encouragement and patience; I'm sure it wasn't easy putting up with the moods of a pregnant woman writing a thesis! I could not have done any of this without you guys.

Table of Contents

1	Introduction	1
1.1	Thesis Overview	4
2	Theory	6
2.1	Introduction	6
2.2	Internal wave equations	6
2.3	Dispersion and polarization relations	9
2.4	Theoretical plane wave transmission	10
2.5	Transmission comparison	12
2.6	Wavepacket transmission	17
3	Experimental Methods	20
3.1	Introduction	20
3.2	Experimental set-up	20
3.3	Stratifications and background profiles	24
3.4	Synthetic schlieren technique	30
3.5	The Hilbert transform	33
3.6	Experimental transmission	38
4	Results	40
4.1	Introduction	40
4.2	Transmissions for oscillating cylinder experiments	40
4.3	Transmissions for rotating disk experiments	47

4.4 Discussion of results	51
5 Conclusions	55
Bibliography	57

List of Tables

4.1	Parameters and errors for oscillating cylinder experiments . . .	45
4.2	Transmission results for oscillating cylinder experiments	46
4.3	Parameters and errors for rotating disk experiments	51
4.4	Transmission results for rotating disk experiments	51

List of Figures

2.1	Transmission across N^2 -barrier	14
2.2	Transmission across weak stratification region	16
3.1	Front view of tank	21
3.2	Rotating disks apparatus	23
3.3	Creating non-uniform stratification	25
3.4	Experimental density profiles	26
3.5	Sensitivity of σ/L to background profile fitting	29
3.6	Synthetic schlieren set-up	31
3.7	Creating vertical time series using synthetic schlieren	32
3.8	Simple 2D Hilbert transform example	34
3.9	Unfiltered and filtered wavefield in Fourier space of simple 2D example	35
3.10	Filtered wavefield in real space of simple 2D example	36
3.11	Experimental example using Hilbert transform filter	37
3.12	Plots of Fourier transformed slices taken above and below the mixed region	39
4.1	Density and squared buoyancy frequency profiles for an oscil- lating cylinder experiment	41
4.2	Hilbert transform applied to vertical time series and snapshot of an oscillating cylinder experiment	42

4.3	Plots of Fourier transformed slices taken above and below the mixed region of an oscillating cylinder experiment	44
4.4	Density and squared buoyancy frequency profiles for a rotating disk experiment	48
4.5	Hilbert transform applied to vertical time series and snapshot of a rotating disk experiment	49
4.6	Plots of Fourier transformed slices taken above and below the mixed region of a rotating disk experiment	50
4.7	Theoretical transmission plot for an oscillating cylinder experiment	52
4.8	Theoretical transmission plot for an oscillating cylinder experiment	53
4.9	Theoretical transmission plot for an oscillating cylinder experiment	54

Chapter 1

Introduction

Internal gravity waves exist in fluid media which experience buoyancy restoring forces due to density stratification. As such, they play an important role in the oceans and atmosphere, whose environments are stably stratified where the effective background density, $\bar{\rho}(z)$, decreases with height. (In the atmosphere stability is appropriately measured by increasing potential temperature with height.) Able to propagate both vertically and horizontally through these stratified fluids, internal gravity waves transport energy and momentum away from their source and deposit them upon breaking.

Within a stratified fluid, internal waves propagate freely with any frequency at or below the natural vertical oscillation frequency of the fluid, N . This is called the buoyancy frequency or the Brunt-Väisälä frequency, defined under the Boussinesq approximation as

$$N^2(z) = -\frac{g}{\rho_0} \frac{d\bar{\rho}}{dz} \quad (1.1)$$

where g is the gravitational acceleration and ρ_0 is the characteristic background density.

Waves with frequency $\omega < N$ propagate freely through the fluid but if the wave's frequency exceeds the buoyancy frequency, $\omega > N$, the waves become 'evanescent disturbances' whose amplitude decays exponentially. Trajectories of internal wave propagation are typically calculated using 'ray tracing' tech-

niques, which applies WKB theory (Lighthill, 1978; Broutman et al., 2004). The WKB approximation assumes that the vertical wavelength of the waves is small compared to the vertical variations of the background density and velocity fields. Heuristics based on ray theory predict that small-amplitude waves will completely reflect from a level z_r where $\omega = N$, and will asymptotically approach a critical level z_c where $\omega = 0$ (Bretherton, 1966). The current study shows that waves with relatively large vertical wavelength are still able to transmit through levels where they would typically be predicted to reflect. This process, called internal wave tunnelling, is analogous to the quantum mechanical process of electron tunnelling.

Internal wave tunnelling has previously been investigated by Eckart (1961) who considered the transfer of vertical wave energy between two regions of locally enhanced stratification in the ocean. The study theoretically examined the transfer of energy in resonant wave modes between the main and seasonal thermoclines. A similar study of the atmosphere was presented by Fritts and Yuan (1989) who looked at resonant energy transfer between the stratosphere and the ionosphere. These studies cannot, however, be used to describe the one-way transfer of energy between two regions of locally enhanced stratification.

The study done by Sutherland and Yewchuk (2004) presents the first laboratory evidence of internal wave tunnelling. Their primary goal was to derive a formula for predicting transmission of internal waves, where transmission is the squared ratio of transmitted to incident wave amplitudes. This formula for plane waves based was on an idealized continuous piecewise-constant $N^2(z)$ profile termed the ‘ N^2 -barrier’. This profile had a finite-depth middle layer of well-mixed to weakly stratified fluid bounded on the top and bottom by layers of uniformly stratified fluid with buoyancy frequency N_0 . This type of profile was an idealization of the background density profiles of the atmosphere

and ocean. In the atmosphere internal waves propagate through the strongly stratified stratosphere and tunnel through the weakly stratified mesosphere to the strongly stratified ionosphere. In the ocean the tunnelling process takes place between the seasonal and main thermoclines. The transmission formula depends on the buoyancy frequency of the fluid, the depth of the well-mixed or weakly stratified layer and the frequency and horizontal wavenumber of the plane wave propagating through the fluid.

Brown and Sutherland (2007) extended this work by considering the addition of a piecewise-linear shear flow to the well-mixed layer. Transmission, in their case, was defined as the flux of transmitted to incident pseudoenergy since wave energy is not conserved due to the presence of shear. They found that for weak shear, maximum transmission occurred for waves propagating at 45° to the vertical. For strong shear, waves could transmit across a critical layer, where the wave speed matched that of the background flow speed.

A numerical technique that computes transmission for internal waves was developed by Nault and Sutherland (2007). This technique directly integrates the Taylor-Goldstein equation for disturbances in a given background stratification and horizontal mean flow. In particular, they considered a fluid with no mean flow and uniform weakly stratified fluid overlaying a uniform strongly stratified fluid with a transition region between the two. For a plane wave propagating upward, from strong to weak stratification, they found that the WKB prediction was accurate if the transition distance between two stratified regions was larger than one sixth the vertical wavelength of the transmitted waves. Here we use their numerical technique to determine the theoretical transmission for tunnelling waves with no background flow.

The current study rigorously explores the experimental work begun by Sutherland and Yewchuk (2004) on internal wave tunnelling through continuously varying background density profiles by completing a detailed analysis

of the oscillating cylinder experiments performed in that study. Additional experiments were conducted using a rotating disk apparatus to generate internal waves. The processes and techniques that we used and developed to measure and compute experimental and theoretical transmission coefficients under nonidealized circumstances are discussed.

1.1 Thesis Overview

In Chapter 2 of this thesis the theoretical background and numerical methods are discussed. We review the theoretical transmission coefficient formula derived by Sutherland and Yewchuk (2004) for plane waves and compare its transmissions to those generated by integrating the Taylor-Goldstein equation. This is followed by our derivation of the formula for transmission coefficients of wavepackets.

Chapter 3 describes our experimental set-up and processing techniques. The experimental set-up sections include how we create a horizontally mixed layer bounded on the top and bottom by strongly stratified fluid and describes the two types of wave generators used. The synthetic schlieren technique is used for visualizing the internal waves in the experiment and is explained in some detail in Section 3.4. Section 3.5 describes the wave-filtering technique using Hilbert transforms. Applying the Hilbert transform in this way allows the separation of rightward from leftward components as well as upward from downward components of the waves. This means that one can retain waves with only the desired horizontal and vertical wavenumbers corresponding to transmitted or reflected waves. This chapter concludes with our derived formula for transmission coefficients as measured directly from the experiments.

Calculations of measured and theoretical transmission coefficients for two specific experiments are outlined in Chapter 4. Tables of transmission coeffi-

cients for all performed experiments are given and a discussion of transmission agreement follows. Conclusions are given in Chapter 5.

Chapter 2

Theory

2.1 Introduction

This section presents the internal wave equations used in this study with a detailed description of the assumptions and simplifications used in their derivation. After discussing previous theory done on transmission of internal waves through tunnelling regions, these ideas will be extended to more geophysically realizable background profiles through application of a numerical code that integrates the Taylor-Goldstein equation to find transmission coefficients. The theory on plane wave tunnelling is then extended to wavepackets, as required for this study.

2.2 Internal wave equations

We start with the fully nonlinear Euler equations, which express the conservation of momentum and mass in the absence of viscosity:

$$\rho_T \frac{D\vec{u}}{Dt} = -\nabla p_T + \vec{g}\rho_T, \quad (2.1)$$

$$\frac{\partial \rho_T}{\partial t} + \nabla \cdot (\rho_T \vec{u}) = 0. \quad (2.2)$$

Here ρ_T and p_T are the total density and pressure, respectively, where p_T is the sum of the background, $\bar{p}(z)$, and fluctuation, $p(\vec{x}, t)$, pressures and ρ_T is the sum of the background, $\bar{\rho}(z)$, and fluctuation, $\rho(\vec{x}, t)$, densities. The velocity

field is denoted by \vec{u} and $\vec{g} = -g\hat{z}$ is the acceleration due to gravity. The fluid is in background hydrostatic balance, so that the ambient buoyancy forces are balanced by the background pressure gradient forces: $\frac{d\bar{p}}{dz} = -\bar{\rho}g$. By using the definition of the material derivative restricting ourselves to the x - z plane and expanding the other terms, we get

$$\rho_T \frac{Du}{Dt} = -\frac{\partial p}{\partial x}, \quad (2.3)$$

$$\rho_T \frac{Dw}{Dt} = -\frac{\partial p}{\partial z} - g\rho, \quad (2.4)$$

$$\frac{D\rho_T}{Dt} = -\rho_T \nabla \cdot \vec{u}. \quad (2.5)$$

For our study, we can also assume that the fluid is incompressible:

$$\frac{D\rho_T}{Dt} = 0. \quad (2.6)$$

Combined with (2.5), we get $\rho_T \nabla \cdot \vec{u} = 0$, or, because ρ_T is strictly positive,

$$\frac{\partial u}{\partial x} + \frac{\partial w}{\partial z} = 0. \quad (2.7)$$

For a salt-stratified liquid, ignoring diffusion, the conservation of substance is again given by (2.6) and this can be written explicitly in terms of its fluctuation and background parts as $\frac{D\rho_T}{Dt} = \frac{D\rho}{Dt} + \frac{D\bar{\rho}}{Dt} = 0$. Since $\bar{\rho}$ is only a function of z , this simplifies to

$$\frac{D\rho}{Dt} = -w \frac{d\bar{\rho}}{dz}. \quad (2.8)$$

A Boussinesq fluid is one in which the density varies slowly with height so that it can be treated as approximately constant except where it is associated with the buoyancy term. Applying the Boussinesq approximation where ρ_0 is the characteristic background density, equations (2.3) and (2.4) become

$$\frac{Du}{Dt} = -\frac{1}{\rho_0} \frac{\partial p}{\partial x}, \quad (2.9)$$

$$\frac{Dw}{Dt} = -\frac{1}{\rho_0} \frac{\partial p}{\partial z} - \frac{g}{\rho_0} \rho. \quad (2.10)$$

Likewise, the assumption that the fluid is incompressible is consistent with the Boussinesq approximation.

Assuming small-amplitude waves means the non-linear advection terms $(\vec{u} \cdot \nabla)$ are small so that they can be neglected. These assumptions reduce the equations to the following coupled set of linear PDEs:

$$\frac{\partial u}{\partial t} = -\frac{1}{\rho_0} \frac{\partial p}{\partial x}, \quad (2.11)$$

$$\frac{\partial w}{\partial t} = -\frac{1}{\rho_0} \frac{\partial p}{\partial z} - \frac{g}{\rho_0} \rho, \quad (2.12)$$

$$\frac{\partial \rho}{\partial t} = \frac{\rho_0}{g} N^2 w, \quad (2.13)$$

$$\frac{\partial u}{\partial x} + \frac{\partial w}{\partial z} = 0, \quad (2.14)$$

where we have defined the squared buoyancy frequency as

$$N^2 = -\frac{g}{\rho_0} \frac{d\bar{\rho}}{dz}. \quad (2.15)$$

Due to the continuity equation for an incompressible fluid (2.14), the horizontal and vertical velocities can be written in terms of the streamfunction, $\psi(x, z, t)$:

$$u = -\partial\psi/\partial z, \quad (2.16)$$

$$w = \partial\psi/\partial x. \quad (2.17)$$

Hence (2.11) and (2.12) become

$$-\frac{\partial^2 \psi}{\partial z \partial t} = -\frac{1}{\rho_0} \frac{\partial p}{\partial x}, \quad (2.18)$$

$$\frac{\partial^2 \psi}{\partial x \partial t} = -\frac{1}{\rho_0} \frac{\partial p}{\partial z} - \frac{g}{\rho_0} \rho. \quad (2.19)$$

We can eliminate p by subtracting the z -derivative of (2.18) from the x -derivative of (2.19) and taking the time-derivative of both sides:

$$\left(\frac{\partial^2}{\partial x^2} + \frac{\partial^2}{\partial z^2} \right) \frac{\partial^2 \psi}{\partial t^2} = -\frac{g}{\rho_0} \frac{\partial^2 \rho}{\partial x \partial t}. \quad (2.20)$$

Combining this equation with the x -derivative of (2.13) gives

$$\left(\frac{\partial^2}{\partial x^2} + \frac{\partial^2}{\partial z^2}\right) \frac{\partial^2 \psi}{\partial t^2} + N^2 \frac{\partial^2 \psi}{\partial x^2} = 0. \quad (2.21)$$

This single PDE describes the structure and evolution of internal waves in stationary stratified fluid with buoyancy frequency $N(z)$.

Since the equation is linear and has coefficients that are independent of x and t the wave structure can be represented by the real part of the streamfunction $\psi = \phi(z) \exp[i(kx - \omega t)]$, in which k is the horizontal wavenumber and ω is the frequency of the wave. Substituting this into (2.21), the streamfunction amplitude, $\phi(z)$, is given by the solution of the Taylor-Goldstein equation (Drazin and Reid, 1981) with no background flow:

$$\phi'' + k^2 \left(\frac{N^2}{\omega^2} - 1\right) \phi = 0. \quad (2.22)$$

Solutions to (2.22) are oscillatory in z if $\omega < N$ and exponential in z if $\omega > N$.

We will focus on solutions of (2.22) where ω is smaller than N in strong stratification, and where ω is larger than N in weak stratification. In our experiments, two regions of strong stratification will be in the upper and lower extremes of the domain and the region of weak stratification will be in the middle of the domain. We will see that this results in the partial transmission and reflection of the waves that are incident upon the weakly stratified fluid in the middle of the domain.

2.3 Dispersion and polarization relations

We now consider the special case of (2.22) where $N = N_0$, a constant:

$$\phi'' + k^2 \left(\frac{N_0^2}{\omega^2} - 1\right) \phi = 0. \quad (2.23)$$

The general solution to (2.23) is

$$\phi(z) = Ae^{imz} + Be^{-imz}, \quad (2.24)$$

where m , if real, is interpreted as the vertical wavenumber and is defined by

$$m^2 = k^2 \left(\frac{N_0^2}{\omega^2} - 1 \right). \quad (2.25)$$

Isolating for ω gives the dispersion relation for internal waves in uniformly stratified Boussinesq fluid:

$$\omega^2 = N_0^2 \frac{k^2}{k^2 + m^2}. \quad (2.26)$$

The polarization relations, which relate the amplitudes of the basic state fields, can be determined from the linearized equations of motion given in (2.11)-(2.14). The following two polarization relations will be useful as reference in this study:

$$A_\xi = -\frac{k}{\omega} A_\psi = -\frac{k}{N_0 \cos \Theta} A_\psi, \quad (2.27)$$

$$A_{N_t^2} = kmN_0^2 A_\psi = k^2 N_0^2 \tan \Theta A_\psi. \quad (2.28)$$

Here ξ is the vertical displacement of the fluid, ψ is the streamfunction as previously defined, $N_t^2 = (-g/\rho_0)\partial^2\rho/\partial z\partial t$ is the time-derivative of the squared buoyancy frequency based upon the total density field and $\Theta \equiv \tan^{-1}(m/k)$ where $-90^\circ \leq \Theta \leq 90^\circ$.

2.4 Theoretical plane wave transmission

In special circumstances (2.22) can be solved analytically. This was done by Sutherland and Yewchuk (2004) who considered transmission across an N^2 -barrier defined by

$$N^2 = \begin{cases} N_0^2, & |z| > L/2 \\ 0, & |z| \leq L/2 \end{cases} \quad (2.29)$$

where the well-mixed region of depth L is centered about $z = 0$ and N_0 is the buoyancy frequency of the stratified fluid outside the well-mixed region. The “ N^2 -barrier” is so-termed because it is directly analogous to the quantum mechanical situation in which a free electron tunnels across a potential barrier.

Solutions of (2.22) above, within and below the barrier are

$$\phi = \begin{cases} A_T e^{i\gamma z}, & z > L/2 \\ A_{UE} e^{z/\delta} + A_{DE} e^{-z/\delta}, & -L/2 < z < L/2 \\ A_I e^{i\gamma z} + A_R e^{-i\gamma z}, & z < -L/2 \end{cases} \quad (2.30)$$

with $\delta = 1/k$ and $\gamma = -k(N_0^2/\omega^2 - 1)^{1/2}$. Here we have assumed the wave is incident from below with amplitude A_I and transmits with amplitude A_T . The amplitudes of the upward- and downward-propagating exponentially decaying (evanescent) waves within the well-mixed region are given by A_{UE} and A_{DE} , respectively. Since upward-propagating waves have negative vertical wavenumber the complex exponential following A_I and A_T in (2.30) have $\gamma < 0$. The reflected downward-propagating wave has positive vertical wavenumber and amplitude, A_R .

The boundary conditions at $z = \pm L/2$ require that the vertical velocity and pressure fields are continuous (Drazin and Reid, 1981). In the Boussinesq approximation with continuous background density and no background flow, this amounts to the condition that ϕ and ϕ' are continuous at $z = \pm L/2$. With (2.30), this results in four equations in five unknowns. Solving to find A_T in terms of A_I gives an explicit formula for the transmission coefficient given by

$$T = \left| \frac{A_T}{A_I} \right|^2. \quad (2.31)$$

This represents the ratio of transmitted to incident energy flux associated with the waves. In stationary fluid with upper and lower stratification the same, as is the case under consideration here, T is equivalently the ratio of transmitted to incident energy. In the same way, the reflection coefficient can

be represented by

$$R = \left| \frac{A_R}{A_I} \right|^2. \quad (2.32)$$

Both T and R will remain unchanged whether A_I and A_T are both amplitudes of streamfunction, ψ , vertical displacement, ξ , or N_t^2 . This is because all three fields are proportional, as shown in (2.27) and (2.28).

Explicitly, for the N^2 -barrier, the transmission coefficient is

$$T = \left[1 + \frac{(\gamma^2 \delta^2 + 1)^2}{(2\gamma\delta)^2} \sinh^2(L/\delta) \right]^{-1}. \quad (2.33)$$

Defining $\Theta = \arccos(\omega/N_0)$ as the angle at which lines of constant phase are oriented from the vertical when $\omega \leq N_0$, and using the definition of δ and γ below (2.30) to (2.33), the transmission coefficient associated with a prescribed incident plane wave is given explicitly by

$$T = \left[1 + \left(\frac{\sinh(kL)}{\sin 2\Theta} \right)^2 \right]^{-1}. \quad (2.34)$$

2.5 Transmission comparison

The numerical solution method of (2.22) for any prescribed $N^2(z)$ was developed by Nault and Sutherland (2007). The incident waves were assumed to be horizontally periodic with given horizontal wavenumber, k , and with fixed frequency, ω . In terms of the streamfunction amplitude of the incident waves, A_I , the code finds the amplitudes of the transmitted and reflected waves, A_T and A_R , respectively.

In order to justify using the integration of the Taylor-Goldstein equation as a theoretical transmission coefficient calculation tool, we first compare it to the analytic transmission formula (2.34) for a range of frequencies and wavenumbers. More generally, we examine transmission across the following smooth analytic function for $N^2(z)$:

$$N^2(z) = N_0^2 + \frac{1}{2}(N_0^2 - N_1^2) \left[\tanh\left(\frac{z - z_u}{\sigma_u}\right) - \tanh\left(\frac{z - z_l}{\sigma_l}\right) \right]. \quad (2.35)$$

Here the parameters σ_u and σ_l represent half the distance over which N^2 changes from one stratification to another. N_0 is the buoyancy frequency of the upper and lower strongly stratified regions and for sufficiently small σ_u and σ_l , N_1 is the buoyancy frequency of the middle weakly stratified region. The values z_u and z_l denote the top and bottom, respectively, of the weakly stratified region occurring at the inflection points of $N^2(z)$.

The N^2 -barrier profile (2.29) is reproduced in the limits $\sigma_u, \sigma_l \rightarrow 0$. While we cannot choose $\sigma_u = \sigma_l = 0$ for use in the code, we can choose them to be arbitrarily small to within floating point digit accuracy.

Figure 2.1 compares transmission coefficients for waves in background $N^2(z)$ profiles given by the piecewise-linear function (a) and the smooth analytic function (b) with $z_u = L/2$, $z_l = -L/2$, $N_1^2/N_0^2 = 0$ and $\sigma_u = \sigma_l = \sigma$. The plot for the piecewise-linear profile is generated using $\sigma/L = 0$ in (2.34) with transmission coefficients given as a function of k and $\omega = N_0 \cos \Theta$. The plot for the smooth analytic profile is generated using $\sigma/L = 0.1$ in the numerical code that computes the transmission coefficients for given k and ω .

The resulting plots are similar both qualitatively and quantitatively. In both cases, transmission coefficients of the plane waves are greatest, in terms of frequency, at about $\omega = N_0/\sqrt{2}$ which corresponds to an angle of propagation from the vertical $\Theta \approx 45^\circ$. This makes intuitive sense: if $\Theta \simeq 0^\circ$, then the incident plane wave is nearly evanescent before encountering the mixed region; if $\Theta \simeq 90^\circ$, then the incident plane wave is propagating nearly horizontally and so ‘sees’ an effectively deeper mixed tunnelling region. Looking at the vertical axis, the transmission increases as the magnitude of kL becomes small. If we consider the case in which the horizontal wavenumber, k , of the plane wave is fixed and we vary the depth of the well-mixed region, L , this means transmission decreases as L becomes large. If $L = 0$, there is no barrier and the fluid is uniformly stratified, so that the plane wave is able to propagate

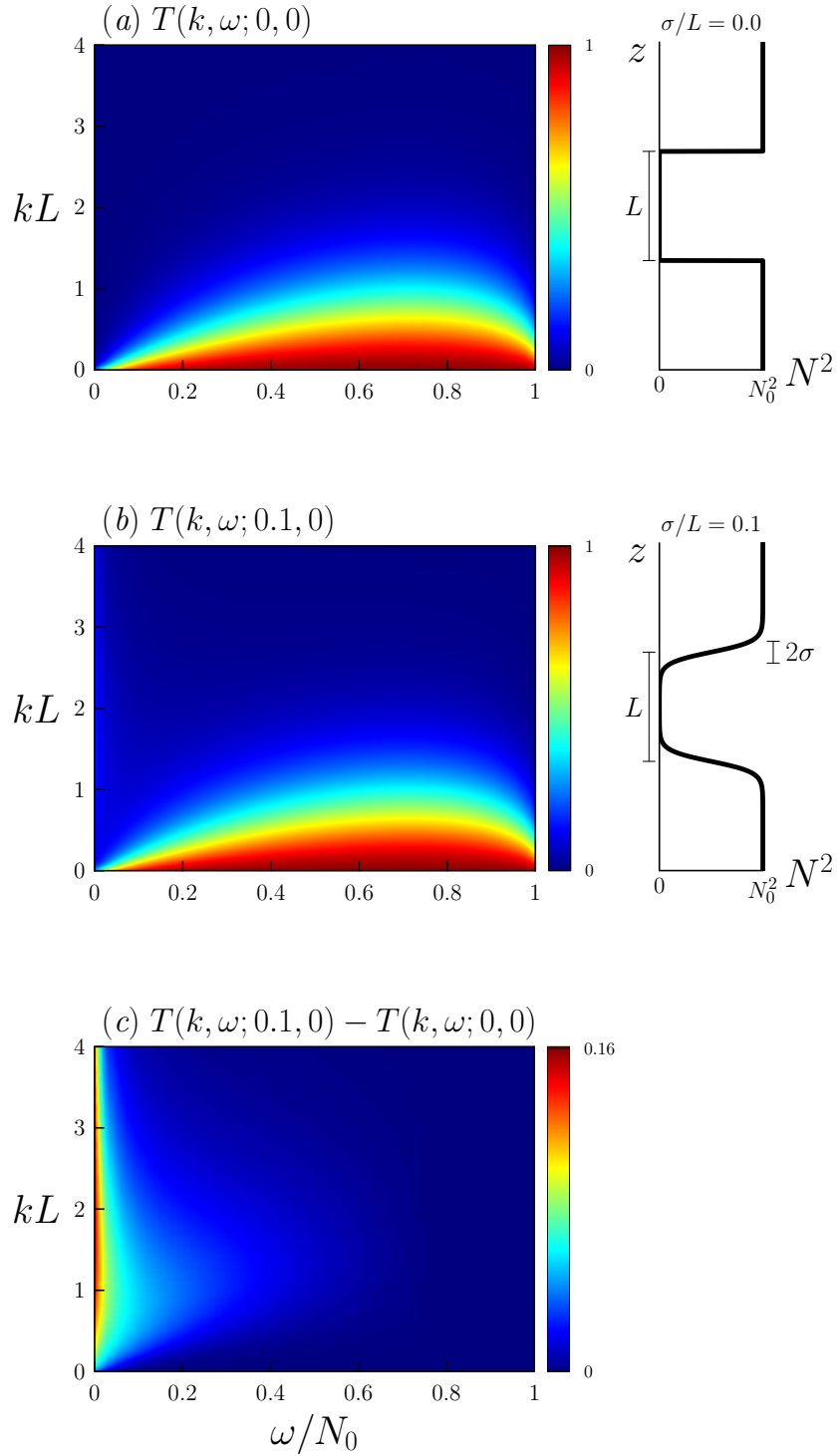


Figure 2.1: Plots of the transmission coefficient $T(k, \omega; \sigma/L, N_1^2/N_0^2)$ computed for (a) the piecewise-linear N^2 profile (2.29) using (2.34), and (b) the smooth analytic N^2 curve (2.35) with $\sigma/L = 0.1$ using the numerical code. The difference in transmission coefficients are given in (c).

freely through the entire fluid. If L is large, the plane wave encountering the well-mixed region becomes evanescent and decays exponentially to negligibly small amplitude before encountering the stratified region on the opposite side. In this case, the transmission coefficient for this plane wave will be close to zero.

Discrepancies between the two transmission plots can be seen by subtracting the two plots, as shown in Figure 2.1(c). Differences on the order of 10% are seen for very small values of ω/N_0 due to the change in σ/L , otherwise, the difference in transmission is negligible. Overall, this is confirmation that integrating the Taylor-Goldstein equation (2.22) gives good agreement with the N^2 -barrier analytic formula when N is given by (2.29). Thus, with greater confidence we can use the Taylor-Goldstein equation to predict theoretical transmissions for other types of N^2 profiles.

One extension of this type of $N^2(z)$ profile which occurs in more realistic circumstances is one where $N_1^2/N_0^2 > 0$, so that the middle region is weakly stratified instead of well-mixed. This is the situation in the atmosphere, in which the weakly stratified mesosphere is bordered by the strongly stratified stratosphere and ionosphere, or in the ocean, where the seasonal and main thermoclines straddle relatively weakly stratified saltwater.

Figure 2.2 compares transmission through an approximately piecewise-linear $N^2(z)$ function to transmission through a smooth analytic profile with $z_u = L/2$, $z_l = -L/2$, $N_1^2/N_0^2 = 0.5$ and $\sigma_u = \sigma_l = \sigma$. The approximately piecewise-linear profile is generated using $\sigma/L = 0.001$. The smooth analytic profile is generated using $\sigma/L = 0.1$.

There are distinct qualitative and quantitative differences between the transmission coefficients as N_1^2/N_0^2 changes from 0.0 to 0.5. There are now two distinct transmission regions, one in the more hydrostatic range ($0 < \omega/N_0 < N_1/N_0$) and one in the more non-hydrostatic range ($N_1/N_0 < \omega/N_0 < 1$).

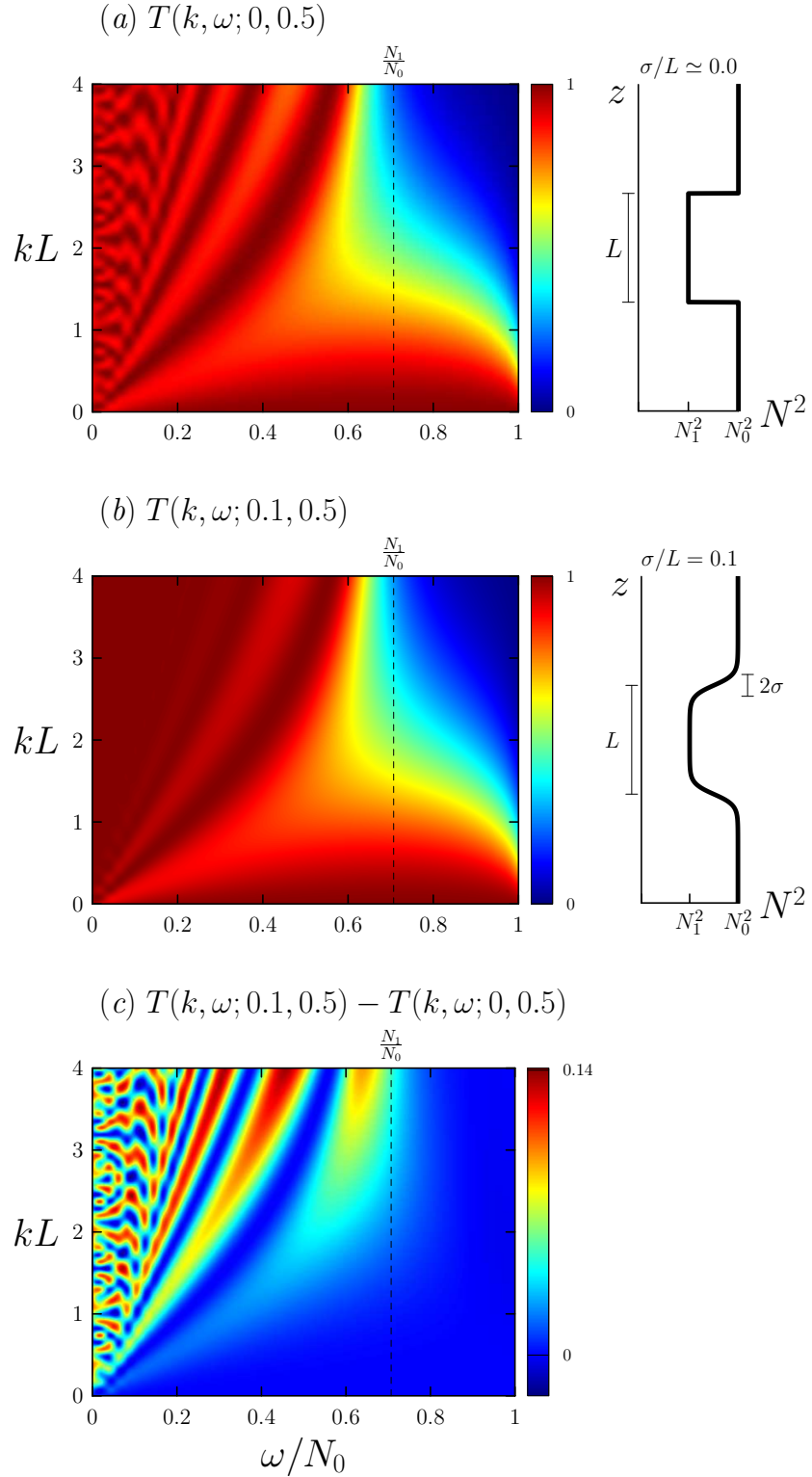


Figure 2.2: Plots of transmission coefficient $T(k, \omega; \sigma/L, N_1^2/N_0^2)$ computed for tunnelling across a weakly stratified region in which $N_1^2/N_0^2 = 0.5$ in the smooth analytic curve (2.35) with (a) $\sigma/L \simeq 0.0$, and (b) $\sigma/L = 0.1$. Both transmission plots are found using the numerical code. The difference in transmission coefficients are given in (c).

When $N_1/N_0 < \omega/N_0 < 1$, the plot exhibits the same behaviour as before where transmission drops off as kL increases. However, when $0 < \omega/N_0 < N_1/N_0$, there is enhanced transmission for all kL . Since the wave frequency is always smaller than the buoyancy frequency in this regime the waves are able to propagate freely through the weakly stratified region. The banded pattern in this range is due to the resonance of certain plane waves within the weakly stratified region. If the vertical wavenumber of the plane wave in the weakly stratified region is an integer multiple of π/L , then the plane wave will resonate within the weakly stratified region, enhancing its transmission.

Between the two regions, where $\omega/N_0 \simeq N_1/N_0$, the transmission changes rapidly for moderate to large values of L . We will refer to this regime as the “transition region”. For waves with characteristics in the transition region, large uncertainties in ω or N_1 lead to large uncertainties in the transmission coefficient.

If σ is non-negligible (Figure 2.2(b)), transmission is enhanced in this banded region because the depth of the weakly stratified region is not as precisely given by L , allowing a greater range of plane waves to be resonant. Also note that the distorted patterns in the very low frequency range of Figure 2.2(a) appear only because of lack of numerical resolution.

2.6 Wavepacket transmission

In previous sections, we have examined the theory for transmission of plane waves. We will now extend this theory to that for wavepackets because the wave generators used in this study produce wavepackets. Assuming the waves are small-amplitude, we can use the fact that wavepackets are a superposition of plane waves to do this.

By Fourier transforming the vertical displacement field, ξ , of the incident waves at a horizontal location prior to reaching the mixed region, the vertical

displacement amplitudes, $A_{\xi n}$, can be extracted. The energy of each plane wave component of the incident wavepacket can be calculated from $\langle E_{In} \rangle = \frac{1}{2}N_0^2|A_{\xi n}|^2$. The energy of the corresponding transmitted components of the wavepacket is $\langle E_{Tn} \rangle = \frac{1}{2}N_0^2|A_{\xi n}|^2T_n$, where T_n are the transmission coefficients associated with each plane wave component of the incident wavepacket. These transmission coefficients are calculated using the numerical code by Nault and Sutherland (2007), as described in Section 2.4.

The total transmission compares the energy of the waves having passed through the mixed region to the energy of the incident waves:

$$T_{\text{thy}} = \frac{\sum_n \frac{1}{2}N_0^2|A_{\xi n}|^2T_n}{\sum_n \frac{1}{2}N_0^2|A_{\xi n}|^2} = \frac{\sum_n |A_{\xi n}|^2T_n}{\sum_n |A_{\xi n}|^2}. \quad (2.36)$$

For the purposes of comparison with experiments, we characterize the wave structure in terms of the time rate of change of the perturbed squared buoyancy frequency

$$N_t^2 = -\frac{g}{\rho_o} \frac{\partial^2 \rho}{\partial t \partial z}. \quad (2.37)$$

By composing a Fourier series of N_t^2 in the horizontal x -dimension, we have in terms of the discrete horizontal wavenumber, k_n , that

$$N_t^2 = \sum_{n=-\mathcal{N}}^{\mathcal{N}} \frac{1}{2} A_{N_t^2 n} e^{ik_n x}. \quad (2.38)$$

Here $k_n = n\frac{2\pi}{\mathcal{L}}$ is the wavenumber of the n 'th mode in a domain of length \mathcal{L} . The maximum modenummer, \mathcal{N} , is set so that $\lambda_{\mathcal{N}} \equiv \frac{2\pi}{k_{\mathcal{N}}} = \frac{\mathcal{L}}{\mathcal{N}}$ is much smaller than the observed characteristic length scale of the wavepacket. The complex amplitude A_n has magnitude equal to the half-peak-to-peak amplitude of the N_t^2 field corresponding to the n 'th mode. The argument of A_n sets the relative phase of the mode. To ensure the field is real, $A_{-n} = A_n^*$, in which the star denotes complex conjugate.

From the polarization relations given in Section 2.3, one can relate the amplitude of the vertical displacement field, A_ξ , to the amplitude of the N_t^2 field for plane waves by

$$A_\xi = -\frac{A_{N_t^2}}{kN_0^3 \sin \Theta}. \quad (2.39)$$

Combining this with (2.36), the transmission coefficient can be defined in terms of amplitudes of the N_t^2 field by

$$T_{\text{thy}} = \frac{\sum_n \frac{1}{k_n^2} |A_{N_t^2 n}|^2 T_n}{\sum_n \frac{1}{k_n^2} |A_{N_t^2 n}|^2} \quad (2.40)$$

where $A_{N_t^2 n}$ is the amplitude of the incident waves of the N_t^2 field in Fourier space and we have assumed that the wavepacket components all have the same frequency, $\omega = N_0 \cos \Theta$.

Chapter 3

Experimental Methods

3.1 Introduction

This section gives a detailed description of the laboratory experiments performed for this study. The tank set-up for internal wave tunnelling is described, including how the mixed region was created and how the density profiles were obtained and fit with a smooth analytic curve. The wavefield was obtained using the image processing technique called ‘synthetic schlieren’ which is described in limited detail. A Hilbert transform was applied to these images in order to filter out certain waves. This method of using the Hilbert transform as an image filtering tool has been newly implemented for internal waves. This section concludes with a description of the formula used for measuring transmission directly from the experiments.

3.2 Experimental set-up

Experiments were performed in a glass tank 197 cm in length, 20 cm in width and 50 cm in height. The tank was filled to a depth of 30 cm or 45 cm with salt-stratified fluid using the standard “double bucket” technique (Oster, 1965). The stratification was made such that the density at the bottom of the tank was approximately 1.05 g/cm^3 and the density at the top of the tank was approximately 1.00 g/cm^3 . A front view schematic of the tank is shown in

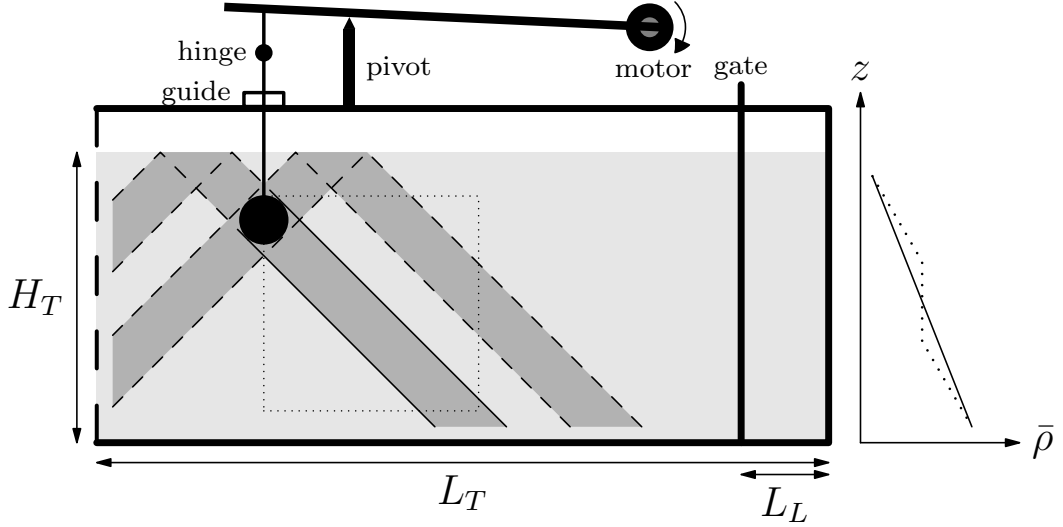


Figure 3.1: Front view of the experimental set-up for the oscillating cylinder experiments. A circular cylinder is vertically oscillated using a motor. A camera is positioned so that the beam propagating downward and to the right, the primary beam, is entirely visible (dotted box). The surface-reflected beams and the beams travelling to the left of the cylinder are not of significance here, as indicated by the long dashed lines. The solid-lined density profile shown on the right is of a typical uniformly stratified fluid and the dotted-lined density profile is of a typical non-uniformly stratified fluid.

Figure 3.1.

A conductivity probe was used to find the background density field, $\bar{\rho}(z)$. It was calibrated by creating anywhere from three to five sample salt concentrations ranging from de-ionized water to the most concentrated solution found in the tank. Their exact concentrations were found using a density meter that is accurate to three decimal places. The vertically descending conductivity probe directly measures the voltage approximately 56 times/cm and, using the calibration solutions, these voltages were converted to densities.

$$\frac{\omega_c}{N} = \cos \Theta. \quad (3.1)$$

To produce internal wave beams, one set of experiments was performed

using a vertically oscillating circular cylinder where the classic cross-pattern of internal waves is generated (Mowbray and Rarity, 1967). This involved vertically oscillating one of two circular cylinders with radii $R = 1.0$ cm and $R = 2.4$ cm. The cylinder was attached to a vertical rod which in turn was attached to the main arm, as shown in Figure 3.1. The main arm was attached to the oscillating motor. A pivot was used to steady the main arm and a guide near the top of the rod was used to keep its oscillations vertical. The cylinder was positioned near the top left side of the tank so that the beam travelling rightward and downward, the primary beam, could be viewed clearly by the camera. The two beams generated by the left side of the cylinder were able to propagate freely and did not interfere with the primary beam. The angle, Θ , of the beams in the cross-pattern is set by the cylinder oscillation frequency, ω_c , relative to N by the relation

$$\frac{\omega_c}{N} = \cos \Theta. \quad (3.2)$$

A second experiment was performed using a variation of an internal wave generator developed by Gostiaux et al. (2007). This device is advantageous because it allows for multiple wavelengths and produces only one arm of the cross-pattern of waves. Having only one beam eliminates the possibility of other beams reflecting off the surface and side walls and interacting with the primary beam. Our apparatus consisted solely of the component of their generator called the camshaft. It was made up of a stack of 17 plastic cylindrical plates, each measuring 14 cm in diameter and 4.8 mm in thickness. A hole was drilled through each disk slightly off-center with a central shaft put through the holes in such a way that the stacked disks formed a helical shape. The disks were arranged so as to create two full vertical wavelengths, each wavelength being 3.60 cm and having a horizontal amplitude of 0.33 cm. The stack of disks extended between the surface of the fluid to 8.1 cm below the sur-

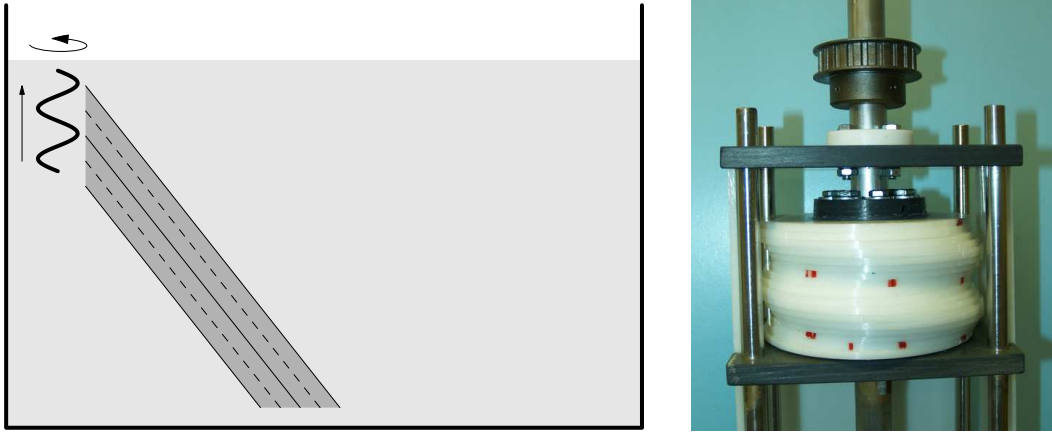


Figure 3.2: Tank schematic and photograph of the rotating disks apparatus. The disks are rotated in a counter-clockwise direction producing a beam with two full vertical wavelengths propagating downward and to the right.

face. The side view profile of the generator had a sinusoidal geometry so that spinning it on its vertical axis forced the sinusoid to move either upward or downward, depending on the direction of rotation.

For our purposes, the disks were rotated in a counter-clockwise sense so that the side profile of the disks moved upwards. Due to the axisymmetric geometry of the generator, the rotating disks produced a conical pattern of downward-propagating waves, consistent with the fact that the vertical group velocity of internal waves is oppositely signed from the vertical phase speed. Once placed at the left end of the tank, additional walls were put around the disks on the three sides preventing waves from travelling in the y -direction or negative x -direction. This ensured that we obtained a single primary beam propagating in the positive x -direction, which we assume is approximately uniform in the y -direction.

3.3 Stratifications and background profiles

In order to study the tunnelling effect, we needed to be able to produce background density profiles with two outer strongly stratified regions and one middle mixed or weakly stratified region. This is set up by placing a gate on the right side of the tank situated 18.5 cm or 14.5 cm from the right wall and mixing the fluid behind the gate thoroughly (see Figure 3.3(a)). The gate was then vertically removed as carefully and quickly as possible. The fluid behind the gate intruded into the stratified fluid at mid-depth, creating a layer of approximately constant density fluid of about 3 cm in depth for the oscillating cylinder experiments and 4 cm in depth for the rotating disk experiments (see Figure 3.3(b)). For successive runs the procedure was repeated, broadening the depth of the mixed region and decreasing its minimum stratification. The stratification of the mixed region, N_1 , ranged from well-mixed to weakly stratified so that $0 \leq N_1^2 < N_0^2$. Regardless of its stratification, this region will hereafter be referred to as the “mixed region”.

Each experiment has four or more runs, each lasting approximately 100 s, with the first run always being with uniformly stratified fluid. Each run thereafter has an intrusion sent down the middle of the tank so that the depth of the mixed region increases by approximately 3 cm or 4 cm with each successive run. The background density profile, $\bar{\rho}(z)$, is obtained before and after each run of the experiment. Examples of experimental density profiles taken after successive runs of one specific experiment are shown Figure 3.4.

Each non-uniform density profile is then empirically fit to a smooth analytic formula of the following form:

$$\bar{\rho}(z) = \rho_0 + \left(\frac{\rho_0}{g}\right) N_0^2 (z_{\max} - z) - \left(\frac{\rho_0}{2g}\right) (N_0^2 - N_1^2) \times \quad (3.3)$$

$$\left[\sigma_u \ln \left(\cosh \left(\frac{z - z_u}{\sigma_u} \right) \right) - \sigma_l \ln \left(\cosh \left(\frac{z - z_l}{\sigma_l} \right) \right) + z_u - z_l \right]$$

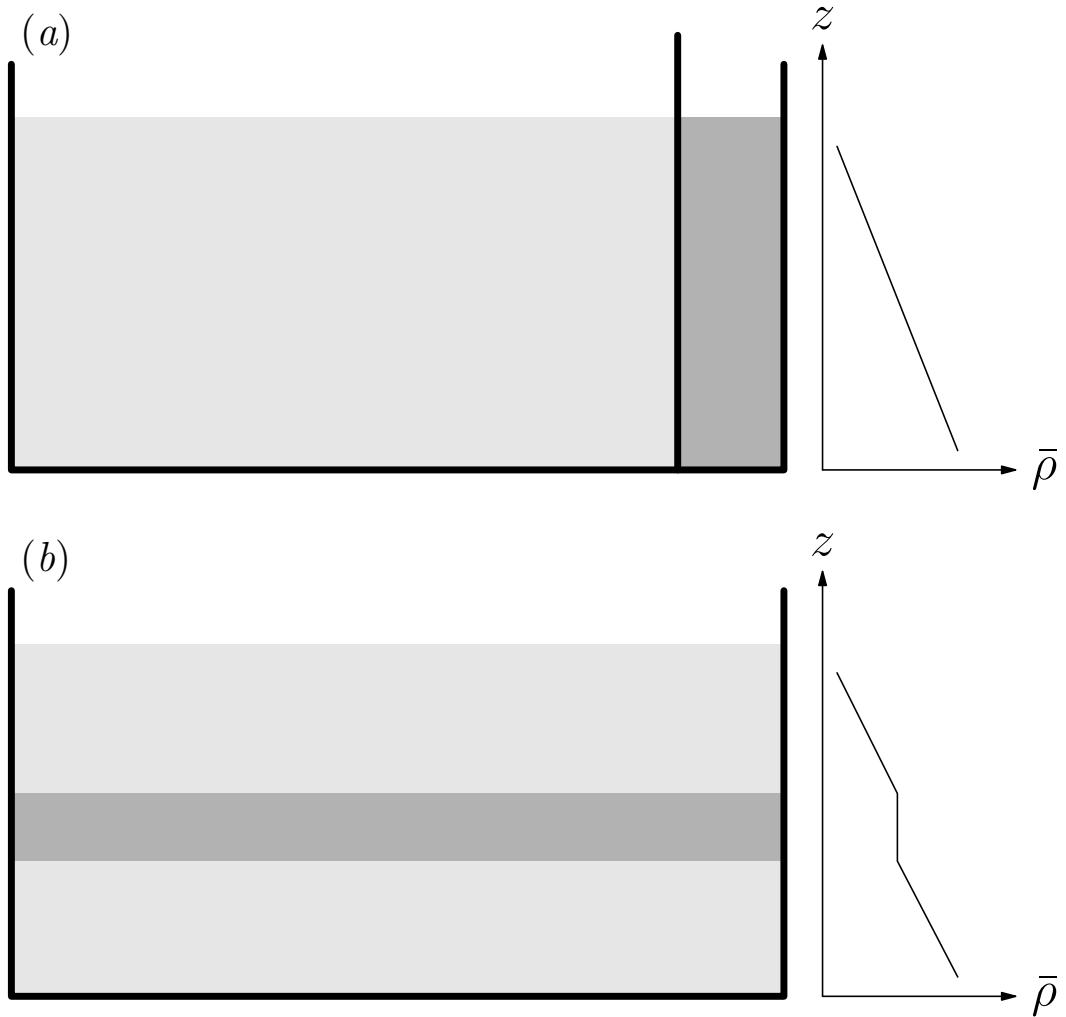


Figure 3.3: Schematic of creating the non-uniform stratification. (a) A gate spanning the width of the tank is inserted to the full depth of the tank and the fluid behind the gate is thoroughly mixed. This uniform density fluid is shown here in dark grey for illustrative purposes. (b) The gate is removed quickly, releasing an intrusive gravity current that propagates down the length of the tank at mid-depth, ultimately creating a non-uniform stratification.

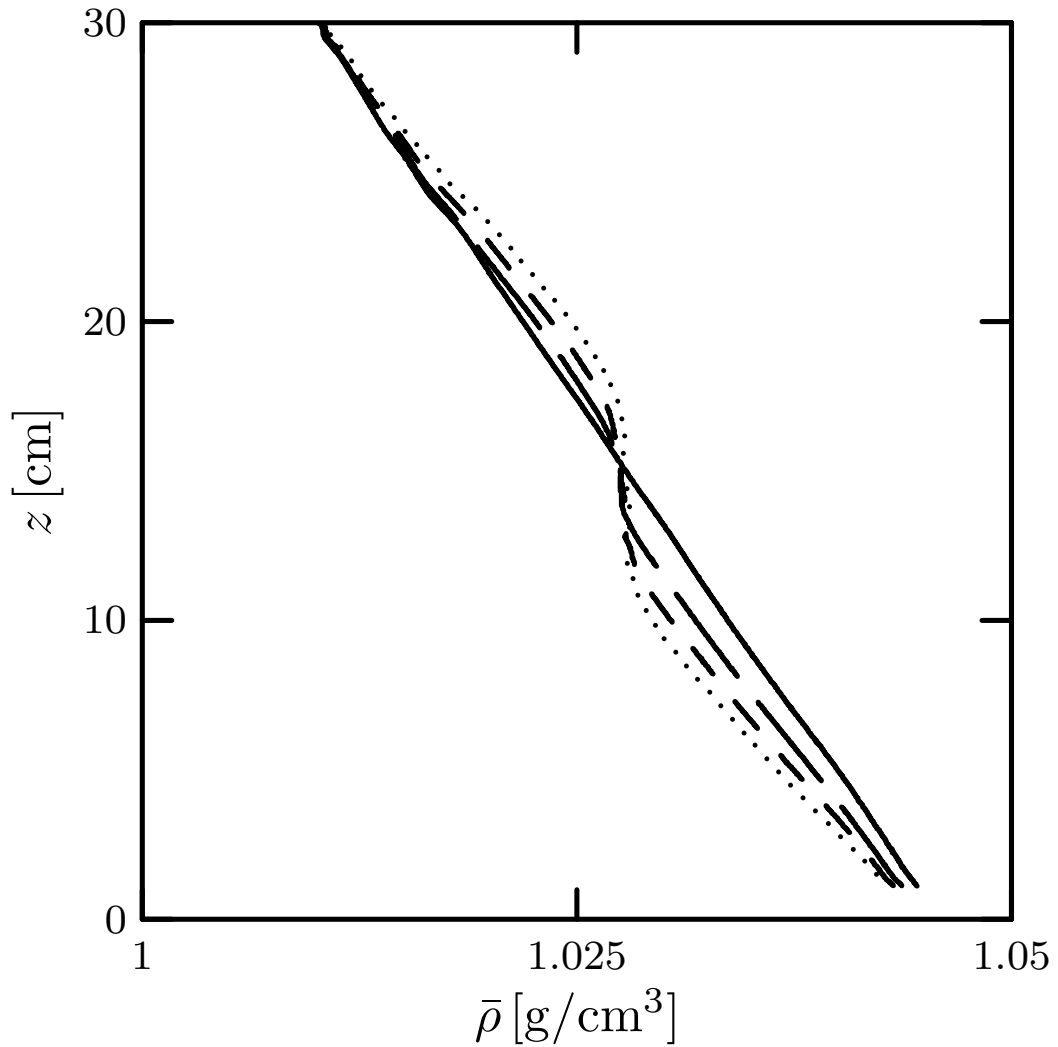


Figure 3.4: Shown are four experimental density profiles. The solid line plots the uniform stratification created by using the double bucket method. The long-dashed, short-dashed and dotted lines plot the density profiles created after repeated intrusions were released at mid-depth so that the depth of the mixed layer increased.

The parameters z_u and z_l indicate the vertical locations of the top and the bottom of the mixed region. σ_u and σ_l are the half-distances over which the stratifications change from the strong to weak, N_1 is the buoyancy frequency of the mixed region and N_0 is the buoyancy frequency of the upper and lower strongly stratified regions. By symmetry of the way in which the mixed region was formed, we assume the upper and lower stratifications were the same and also that $\sigma_u = \sigma_l = \sigma$. The $\ln(\cosh(z))$ functions were chosen because their structure formed a good fit to the experimental profiles. Again, ρ_0 is the characteristic density and g is the acceleration due to gravity.

The points of maximum curvature at the edges of the mixed region were used to find z_u and z_l . N_0 and N_1 were found from the slope of the best-fit lines to their respective regions of the density profile. The slope for N_0 was always calculated from the upper stratified region because certain experiments had errors in the conductivity probe measurements from over-saturation in the lower stratified region. Looking at the density profiles for experiments where the conductivity probe functioned properly throughout the traverse, the buoyancy frequencies in both strongly stratified regions were very close. From the definition of the squared buoyancy frequency,

$$N^2(z) = -\frac{g}{\rho_0} \frac{d\bar{\rho}}{dz}, \quad (3.4)$$

we can make (3.3) into an equation for $N^2(z)$, as used in Section 2.5:

$$N^2(z) = N_0^2 + \frac{1}{2}(N_0^2 - N_1^2) \left[\tanh\left(\frac{z - z_u}{\sigma_u}\right) - \tanh\left(\frac{z - z_l}{\sigma_l}\right) \right]. \quad (3.5)$$

In ideal circumstances, the density profiles obtained from the conductivity probe would be smooth and so would be used to calculate N^2 directly by taking its derivative and multiplying by $-g/\rho_0$. Since the density profile measured in discrete steps by the probe was not smooth their empirical fits to (3.3) are necessary.

Fits to (3.3) were performed by eye for each experimental density profile and the resulting parameters, $N_0, N_1, z_u, z_l, \sigma_u$ and σ_l , were plugged into (3.5). The N^2 profiles from before and after a given run were averaged and the resulting N^2 profile was used in the numerical code to find transmission coefficients.

When using a smooth analytic function like (3.5) to find transmission coefficients, it is important to gain a quantitative understanding of its sensitivity to the parameters involved. For example, when choosing the parameter σ , one must also consider its relationship to N_1^2 . Figure 3.5 shows this relationship. If σ/L is small, the curve attains the desired N_1^2 value at mid-depth. As σ/L is increased the analytic function is unable to attain the desired N_1^2 accurately while keeping the other parameters fixed. This is illustrated in Figure 3.5(c). With $\sigma/L \gtrsim 0.2$, (3.5) does not produce an $N^2(z)$ profile with a minimum close to N_1^2 . Changing the width σ above $0.2L$ changes the value of N_1^2 significantly so as to affect plane wave transmission. Henceforth, the attained value for N_1^2 using the smooth analytic function will be referred to as N_{thy}^2 . In part, we will estimate the error in fitting (3.3) to the measured density profile by the difference in the measured value of N_1^2 and N_{thy}^2 .

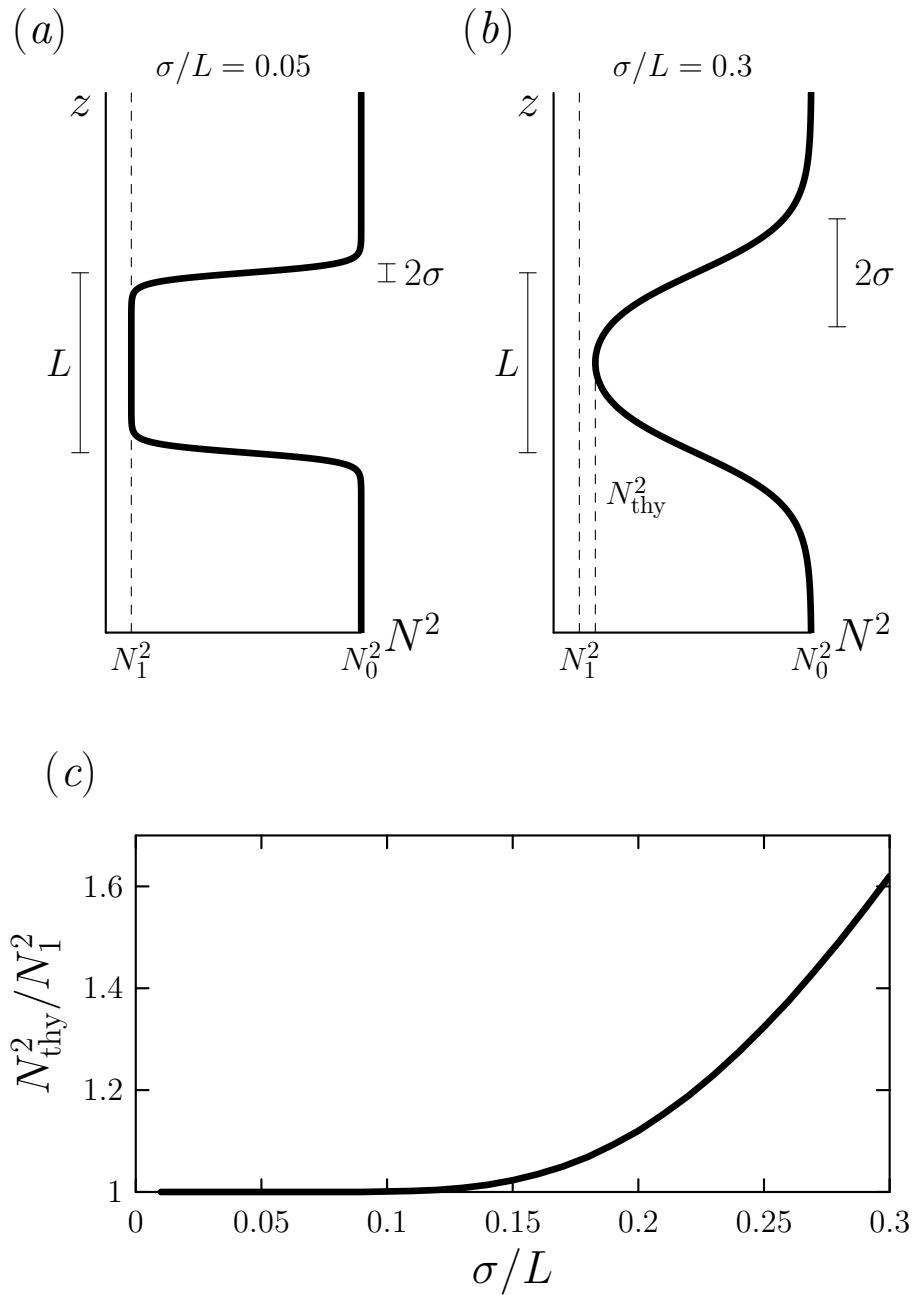


Figure 3.5: Plots of sensitivity to σ/L . Using the smooth analytic function (3.5), both profiles (a) and (b) are created using the same parameters except in (a) where $\sigma/L = 0.05$ and (b) where $\sigma/L = 0.3$. The ratio of N_1^2 to N_{thy}^2 with respect to σ/L is shown in (c).

3.4 Synthetic schlieren technique

In order to look at the internal waves in the tank, the 2D ‘synthetic schlieren’ method (Sutherland, 2002) was used. This method requires that a sheet of horizontal black and white lines be placed behind the salt-stratified tank. A bank of horizontal fluorescent tubes is positioned behind the black and white lines in order to illuminate them for the camera, as shown in Figure 3.6.

As internal waves propagate through the stratified fluid they cause the isopycnals to move up and down. From the viewpoint of the camera, this causes the refractive index of the fluid at a given location to change so that the black and white lines distort. Based on these distortions, the synthetic schlieren processing is able to measure changes in the density gradient non-intrusively.

In both sets of experiments, a camera recording at 30 frames per second was placed at an approximate distance of 280 cm from the front of the tank. The camera’s field-of-view was the region to the right and below the cylinder or rotating disks. This produced an image of approximately 30 cm by 30 cm for the oscillating cylinder experiments and 40 cm by 50 cm for the rotating disk experiments, depending on the zoom of the camera. For all experiments the resolution was approximately 15 pixels/cm in both spatial directions.

The recorded film of the xz -plane was processed using the image processing software package, Digimage (Dalziel et al., 2000). The synthetic schlieren technique calculates differences in the black and white lines (Figure 3.7(a)) from the undisturbed fluid to find the Δz field. The program is then able to create vertical time series at any desired horizontal location in the camera’s view (Figure 3.7(b)). A fixed number of equally spaced vertical time series were taken from each run of the experiment: 28 for the oscillating cylinder experiments and 42 for the rotating disk experiments. For each run of each

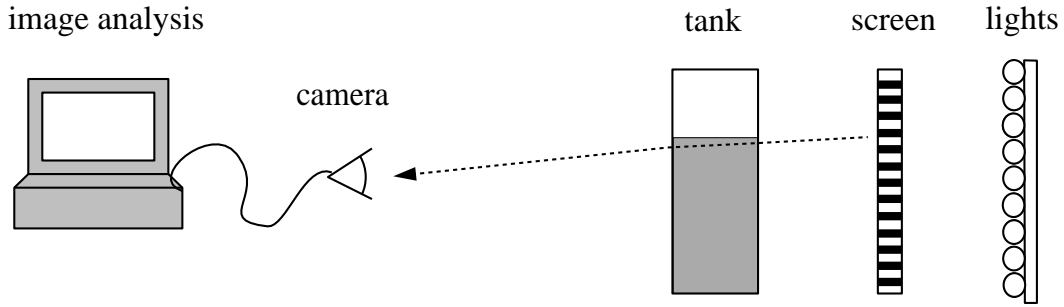


Figure 3.6: Side view of the experimental configuration for the synthetic schlieren technique. The camera records distortions of the image of horizontal lines due to density fluctuations within the fluid. These density fluctuations are the result of internal wave propagation.

experiment, the frequency of the cylinder, ω_c , was found from the vertical time series that intersects the cylinder or edge of the rotating disks. This frequency was assumed to be the frequency of the waves in the wavefield.

For the purposes of this study, it is useful to cast the field of the vertical time series in terms of the time rate of change of the squared buoyancy frequency due to waves, N_t^2 , as shown in Figure 3.7(c). This has the effect of removing long timescale changes within the tank, such as gradual warming of the fluid over the course of the experiment. From numerous vertical time series, a spatial snapshot of the N_t^2 field can be constructed, as seen in Figure 3.7(d).

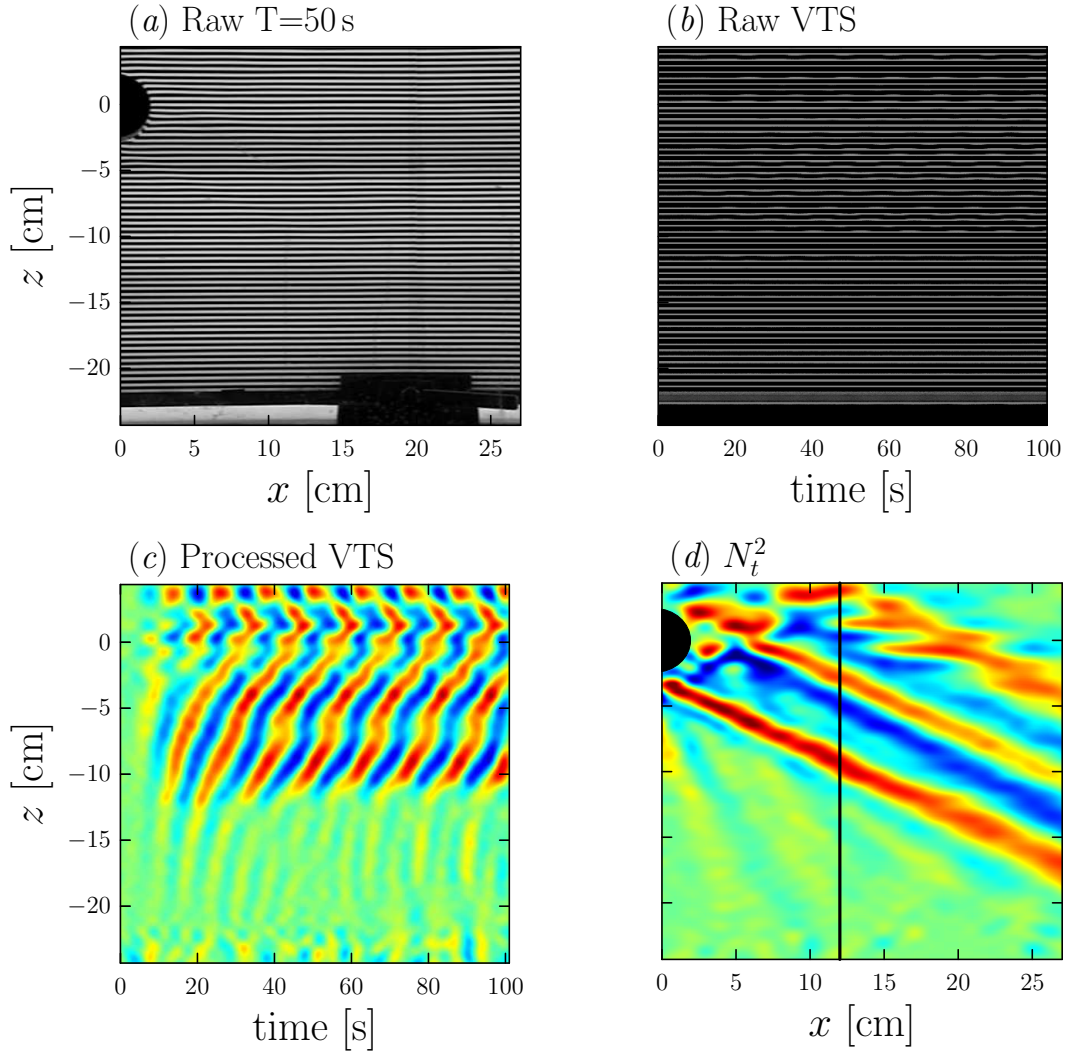


Figure 3.7: (a) A raw image from an oscillating cylinder experiment taken at time $T=50$ s. (b) A raw vertical time series at 12 cm to the right of the center of the cylinder, and (c) its processed N_t^2 vertical time series. (d) A snapshot of the processed N_t^2 field. The vertical line in (d) indicates the location of the vertical time series.

3.5 The Hilbert transform

The Hilbert transform is used in mathematics with applications to signal processing. Mathematically, this transform takes a function and shifts its phase by 90° , thus putting a real function into the imaginary plane. Previous studies have used the Hilbert transform on roll waves and hydrothermal travelling waves to demodulate the signal (Croquette and Williams, 1989; Garnier et al., 2003). The Hilbert transform has recently been applied to internal gravity waves as a technique for separating the four beams emanating in a cross-pattern from an oscillating source (Mercier et al., 2008). As in their work, what we refer to as the ‘‘Hilbert transform’’ is the operation mapping the original real-valued field, f , into a complex-valued field, \tilde{f} , from which upward- or downward-propagating waves can be extracted.

To illustrate the method, we consider the following 2D example of two added plane waves with the specified amplitudes, $A_{1,2}$, vertical wavenumbers, $m_{1,2}$, and frequencies, $\omega_{1,2}$, given mathematically as

$$f(z, t) = A_1 \sin(m_1 z - \omega_1 t) + A_2 \cos(m_2 z - \omega_2 t), \quad (3.6)$$

and shown pictorally in Figure 3.8 where $A_1 = 2$, $A_2 = 3$, $m_1 = 1$, $m_2 = -1$, $\omega_1 = \omega_2 = 0.5$.

From this example, we will show how to extract from a wavefield consisting of superimposed waves only those waves having positive vertical wavenumber (downward-propagating waves).

The numerical code takes the real field, $f(z, t)$, and Fast Fourier Transforms it in space and time creating the transformed field, $\hat{f}(m, \omega)$, which is in vertical wavenumber-frequency space. For example (3.6) we find:

$$\hat{f}(m, \omega) = \begin{cases} -(i/2)A_1, & m = m_1, \omega = \omega_1 \\ (i/2)A_1, & m = m_1, \omega = -\omega_1 \\ (1/2)A_2, & m = m_2, \omega = \omega_2 \\ (1/2)A_2, & m = m_2, \omega = -\omega_2 \\ 0, & \text{otherwise} \end{cases} \quad (3.7)$$

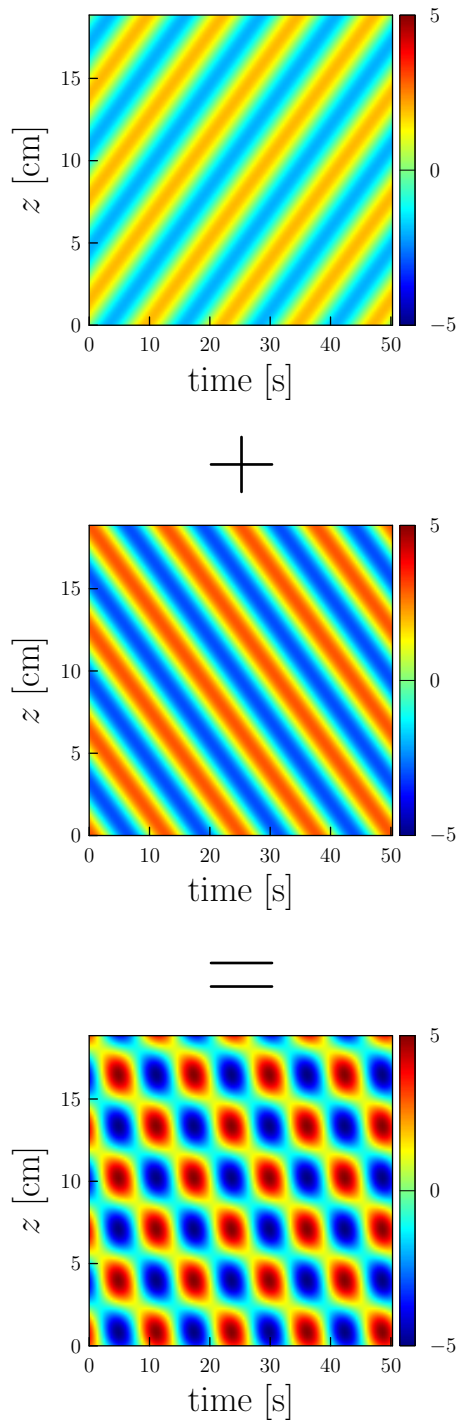


Figure 3.8: As a simple example of the 2D Hilbert transform procedure, we add two plane waves periodic in space and time. For clarity, the plane waves are given different amplitudes and are travelling in opposite vertical directions. The resulting image is used as the starting point for the Hilbert transform procedure.

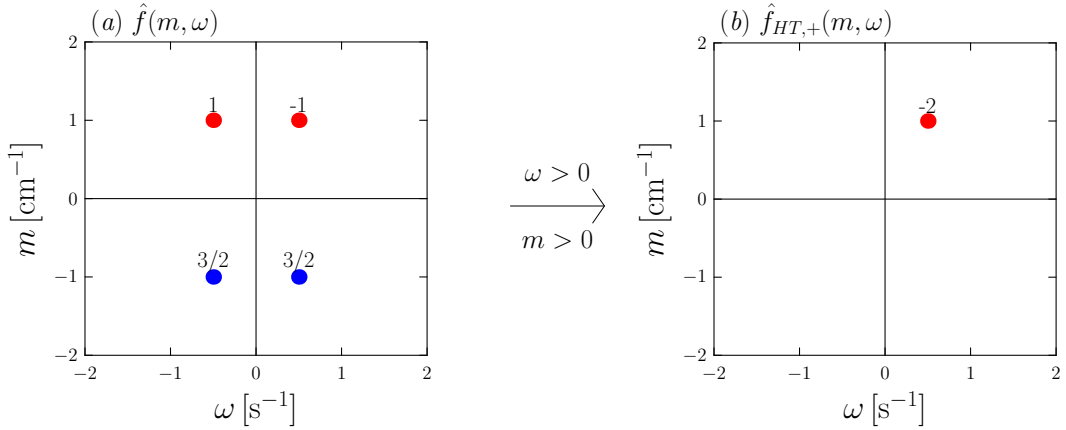


Figure 3.9: Plots of Hilbert transform filtering technique. (a) A plot of the space-time Fourier transform of original image. The red dots denote the imaginary parts of the Fourier transform and the blue dots denote the real parts of the Fourier transform with their respective amplitudes above them. (b) Applying a filter keeping only waves travelling forward in time and waves with positive vertical wavenumber.

as illustrated in Figure 3.9(a).

Now that the signal is in m - ω space, we can begin filtering out the parts of the signal we do not want. We will first focus on the frequency part of the signal where we will keep only the waves travelling forward in time, $\omega > 0$. This step removes exactly half of the energy of the signal, so the Fourier amplitudes of the remaining waves must be multiplied by a factor of two in order to preserve the amplitude of the original signal.

We next focus on the vertical wavenumber part of the signal where we choose to keep either positive or negative vertical wavenumbers. Since our goal was to retain downward-propagating waves, we will take out any part of the signal with negative vertical wavenumbers, keeping $m > 0$. Having appropriately modified the frequencies and vertical wavenumbers in Fourier space, we have now obtained $\hat{f}_{HT,+}(m, \omega)$. For our example,

$$\hat{f}_{HT,+}(m, \omega) = \begin{cases} -iA_1, & m = m_1, \omega = \omega_1 \\ 0, & \text{otherwise.} \end{cases} \quad (3.8)$$

This is illustrated in Figure 3.9(b).

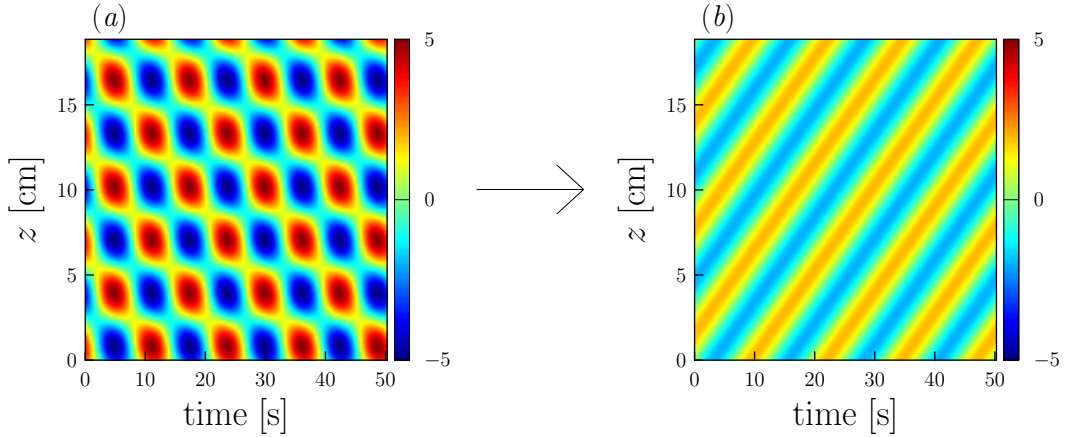


Figure 3.10: (a) Unfiltered original signal. (b) Taking the real part of the inverse Fourier transform of $\hat{f}_{HT,+}(m, \omega)$, we get back the plane wave from our original signal whose vertical wavenumber is positive.

By inverse Fourier transforming this modified field, we obtain the complex-valued field, $\tilde{f}(z, t)$. The real part of this complex signal will be the desired filtered wavefield. In our simplified example, the real part of $\tilde{f}(z, t)$ is $\text{Re}\{-2i \sin(z - 0.5t)\} = 2 \sin(z - 0.5t)$ as expected (see Figure 3.10).

Next we give an example of applying the Hilbert transform to data from a laboratory experiment in which internal waves generated by rotating disks partially transmit through a weakly stratified region. Figure 3.11 illustrates (a) the full wavefield and the field after being separated into waves with (b) positive vertical wavenumber (downward-propagating beam) and (c) negative vertical wavenumber (upward-propagating beam).

For the purposes of our study, we will keep only waves with positive vertical wavenumber, thereby removing upward-propagating beams. This means that the part of the primary beam that reflects off the mixed region is removed as well as the transmitted beam after it reflects off the bottom of the tank. The procedure thus helps us to measure the transmission of the downward-propagating beams.

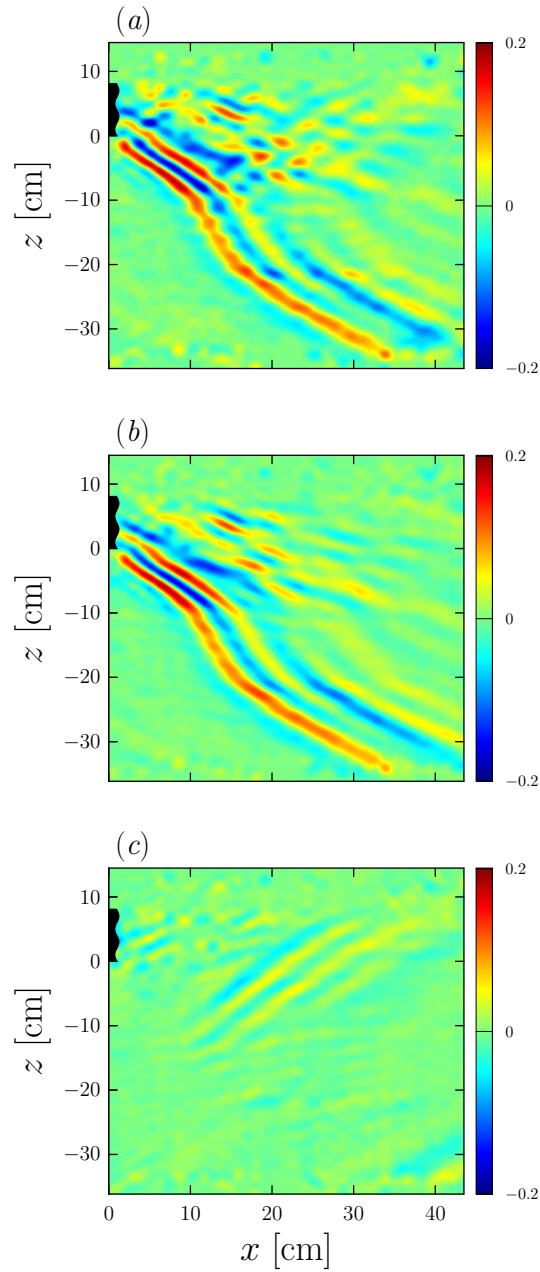


Figure 3.11: Experimental example using the Hilbert transform. (a) The unfiltered experimental image of an internal wave beam generated by the rotating disks tunnelling through a weakly stratified region. The image is filtered to show only those waves with (b) positive vertical wavenumber and (c) negative vertical wavenumber.

3.6 Experimental transmission

In Section 2.6 we derived the theoretical formulae for calculating wavepacket transmission coefficients from its plane wave components. We would like to compare these to experimentally measured transmission coefficients.

The measured transmission coefficients in experiments, corresponding to (2.36), is given by

$$T_{\text{exp}} = \frac{\sum_n \frac{1}{k_{T,n}^2} |A_{T,N_t^2 n}|^2}{\sum_n \frac{1}{k_{I,n}^2} |A_{I,N_t^2 n}|^2} \quad (3.9)$$

where $k_{I,n}$ and $A_{I,n}$ are the horizontal wavenumbers and amplitudes of the incident plane wave components of the wavepacket and $k_{T,n}$ and $A_{T,n}$ are the horizontal wavenumbers and amplitudes of the transmitted plane waves. As in the theoretical calculations, we have assumed that the wavepacket components all have the same frequency as the cylinder, $\omega_c = N_0 \cos \Theta$.

Snapshots of the filtered N_t^2 wavefield are taken once the primary beam has reached steady state. For the oscillating cylinder experiments, steady state is reached at four buoyancy periods of the cylinder and at ten buoyancy periods for the rotating disk experiments. Horizontal slices are taken through the snapshot above and below the mixed region at $z_u + \sigma$ and $z_l - \sigma$, respectively. Taking these slices a distance σ away from the mixed region ensures that an unobstructed signal of the wave structure is captured.

Fourier transforms of these horizontal slices are taken, obtaining k_n and A_n above and below the mixed region. Since the size and resolution of the domain in each case is the same, then $k_{I,n} = k_{T,n}$. The Fourier transform represents a real signal as the sum of its positive wavenumber parts plus the complex conjugate. So the positive wavenumber alone has half the amplitude of the corresponding real signal. Thus we double the amplitude from the FFT routine before computing $|A_{N_t^2 n}|^2$ in (3.9).

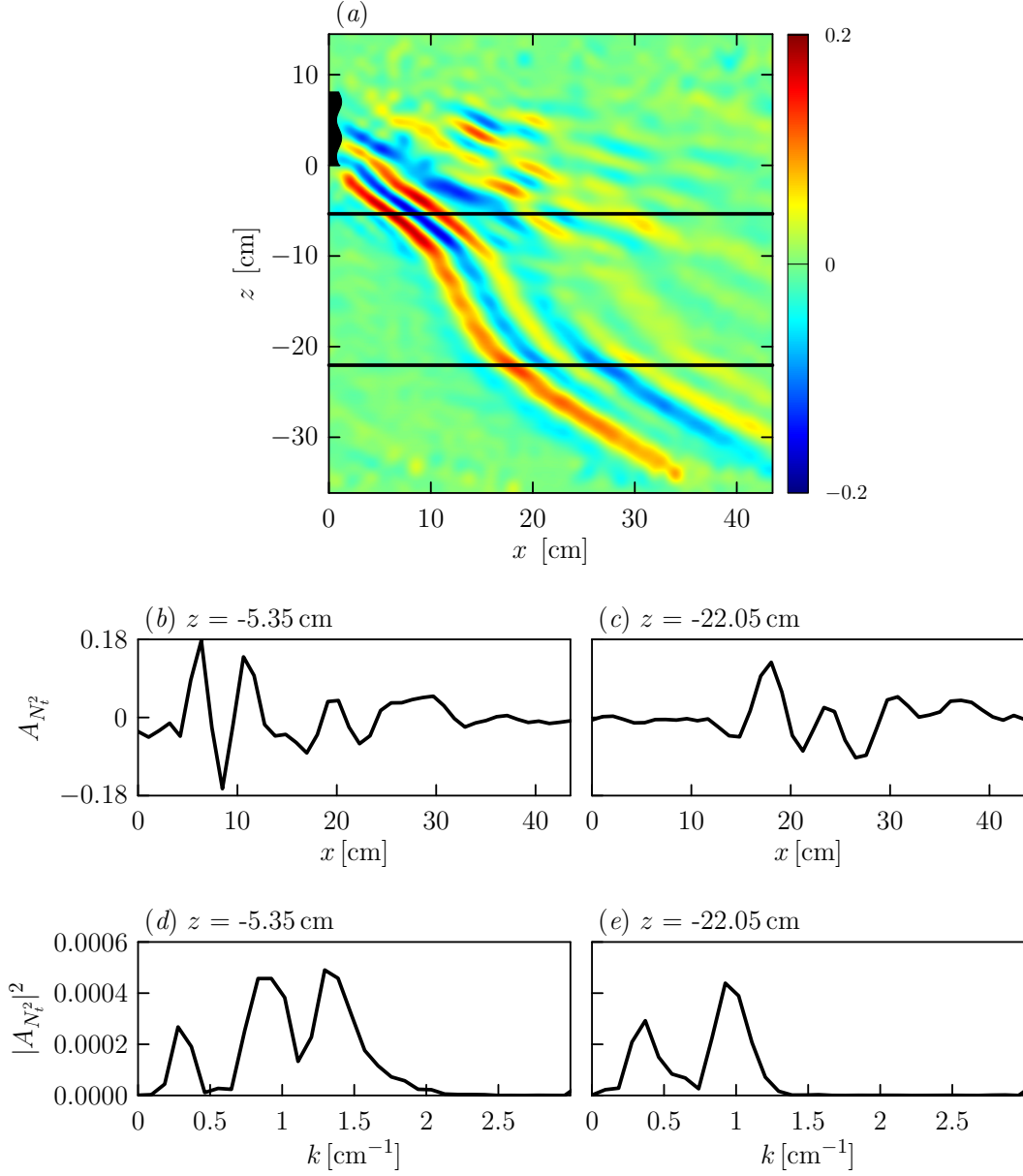


Figure 3.12: (a) A Hilbert filtered snapshot of a beam generated by the rotating disks, tunnelling through a weakly stratified region. (b) A horizontal slice taken above the weakly stratified region at $z_u + \sigma$ and its corresponding Fourier transform, (d). (c) A horizontal slice taken below the weakly stratified region at $z_l - \sigma$ and its corresponding Fourier transform, (e). For this experiment, $z_u = -6.85$ cm, $z_l = -20.55$ cm and $\sigma = 1.5$ cm.

Chapter 4

Results

4.1 Introduction

This chapter gives a detailed review of the procedure used in finding experimental and theoretical transmission coefficients for the oscillating cylinder and rotating disk experiments. The parameters and transmission coefficients for all experiments are given in Tables. A discussion follows on the origin of the discrepancies between experimental measurements and theoretical calculations.

4.2 Transmissions for oscillating cylinder experiments

We begin by showing the results of an experiment in which a cylinder with radius $R = 2.43$ cm is vertically oscillated at a frequency $\omega_c = 0.50$ s⁻¹ with half peak-to-peak amplitude of $A = 0.43$ cm.

After a single intrusion acts partially to mix the tank at mid-depth, we measure the density profile and use (3.3) to fit a smooth curve to it. The resulting parameters for this experiment are found to be $N_0 = 1.11$ s⁻¹, $N_1 = 0.43$ s⁻¹, $z_u = -8.20$ cm, $z_l = -11.40$ cm, $\sigma_u = \sigma_l = \sigma = 0.90$ cm and $\rho_0 = 1.01$ g/cm³. These parameters are put into the squared buoyancy frequency profile (3.5). The background density and N^2 profiles are shown in Figure 4.1. Note that $\omega_c^2 \approx 0.25 \gtrsim N_1^2$. Because $\sigma/(z_u - z_l) \approx 0.28 > 0.2$, we expect

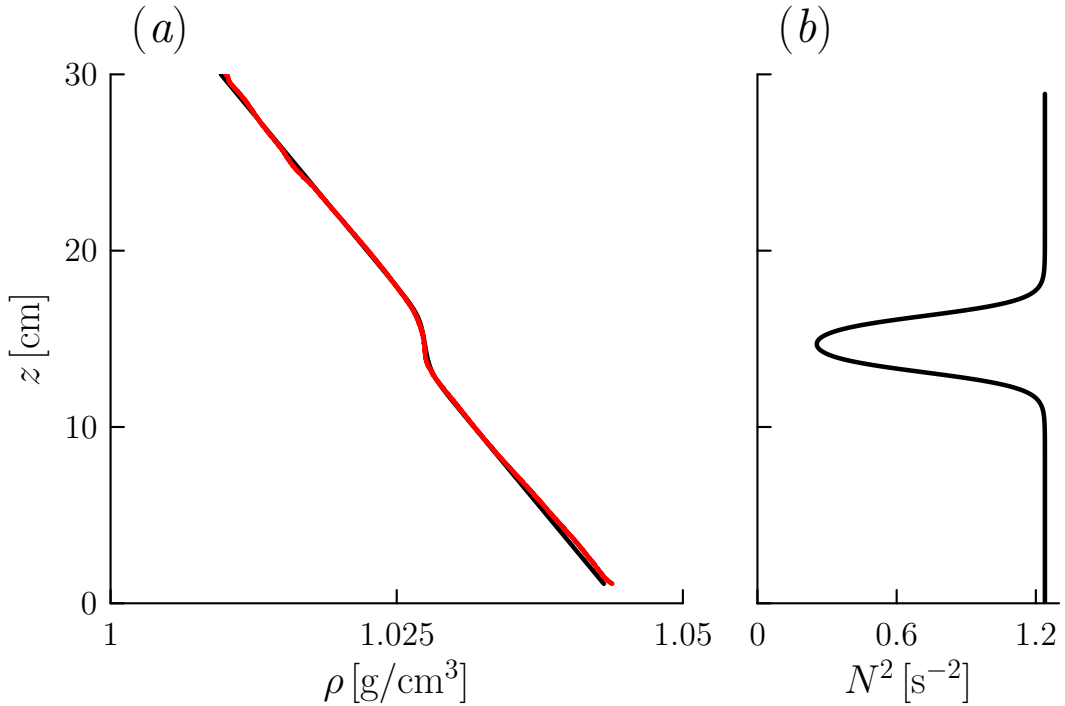


Figure 4.1: Background profiles for an oscillating cylinder experiment. (a) The red curve is the experimental background density profile and the black curve is its smooth analytic fit. (b) The background N^2 profile based on the parameters found for the smooth analytic density profile fit.

some discrepancy between our measured and theoretical values of N_1 and N_{thy} . Nonetheless, Figure 4.1(a) shows good agreement.

From the raw images captured by the camera, the synthetic schlieren process described in Section 3.4 is used to construct processed vertical time series of the N_t^2 field at 28 equally spaced horizontal locations spanning the domain. An N_t^2 snapshot taken after four buoyancy periods (time $\simeq 50$ s) and constructed from these vertical time series is shown in Figure 4.2(b), along with one of its vertical time series in Figure 4.2(a). The Hilbert transform is applied to each of the vertical time series, (Figure 4.2(c)), so that the filtered N_t^2 snapshot shows only the downward-propagating wave (Figure 4.2(d)).

In order to gather information about the horizontal wavenumbers, k_n , and amplitudes, A_n , of the plane wave components entering and exiting the mixed region we will use the ideas from Section 3.6. A horizontal slice of the N_t^2

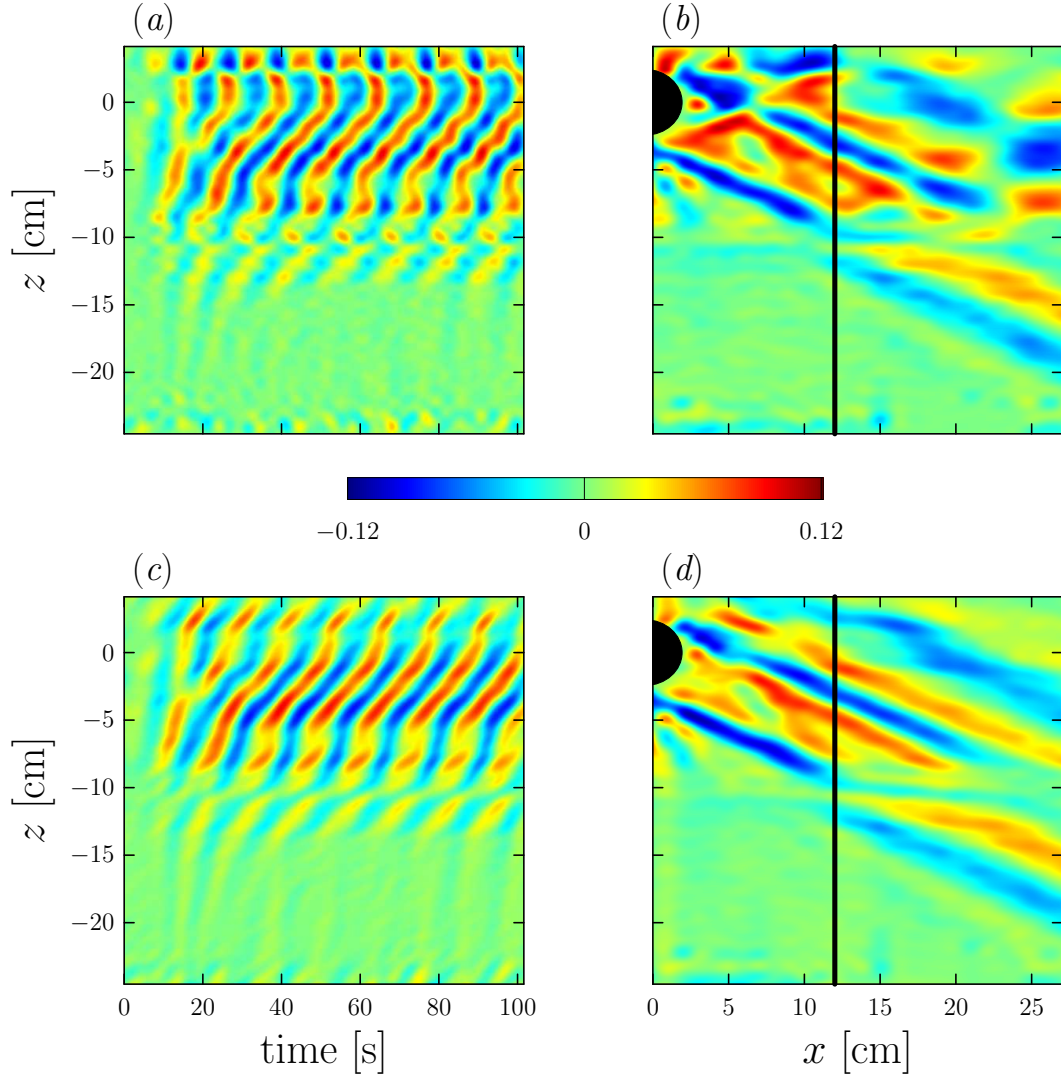


Figure 4.2: A vertical time series taken at $x = 12.01$ cm from the center of the cylinder is shown in (a). 28 of these vertical time series are used to reconstruct at snapshot of the N_t^2 field, (b), at time=50 s. Using the Hilbert transform to filter out $m < 0$ from each vertical time series, (c), a clean view of the downward travelling beam can be seen in (d). All plots have been smoothed for ease of viewing.

snapshot above the mixed region is taken at $z_u + \sigma = -8.20 \text{ cm} + 0.90 \text{ cm} = -7.30 \text{ cm}$, and a horizontal slice below the mixed region is taken at $z_l - \sigma = -11.40 \text{ cm} - 0.90 \text{ cm} = -12.30 \text{ cm}$, where $z = 0$ is the center of the cylinder. A Fourier transform in the x -direction is performed on both slices (Figure 4.3(*b,c*)) resulting in a plot of Fourier amplitudes for plane waves with discrete horizontal wavenumbers. Typically we find the horizontal wavenumber spectrum peaks around a characteristic value $k_c \approx \frac{2\pi}{4R} \cos \Theta$, consistent with theory (Hurley and Keady, 1997).

The amplitudes and horizontal wavenumbers from the upper (incident) and lower (transmitted) horizontal slices were then used to calculate the experimental transmission coefficient of the beam from (3.9).

The theoretical wavepacket transmission coefficient was calculated using (2.40) in which the same incident horizontal wavenumbers and amplitudes of each plane wave component were put directly into the sum and the corresponding transmission coefficients were calculated using the code described in Section 2.4. The parameters used in the oscillating cylinder experiments are recorded in Table 4.1 and their experimental and theoretical transmission coefficients are compared in Table 4.2. The particular experiment shown in Figure 4.2 is denoted “1b”.

This analysis was performed on all available oscillating cylinder experiments for which $0.3 < \omega_c/N_0 < 0.5$. Any experiment conducted which resulted in $\omega_c/N_0 < 0.3$ produced a primary beam whose angle to the vertical was so large ($\Theta \gtrsim 70^\circ$) that the transmitted beam was outside the camera’s field of view. Any experiment which resulted in $\omega_c/N_0 > 0.5$ produced an upward-propagating beam emanating from the cylinder which reflected off the surface of the water only to be in such close proximity to the primary downward-propagating beam emanating from the cylinder so as to obscure the structure of the primary beam.

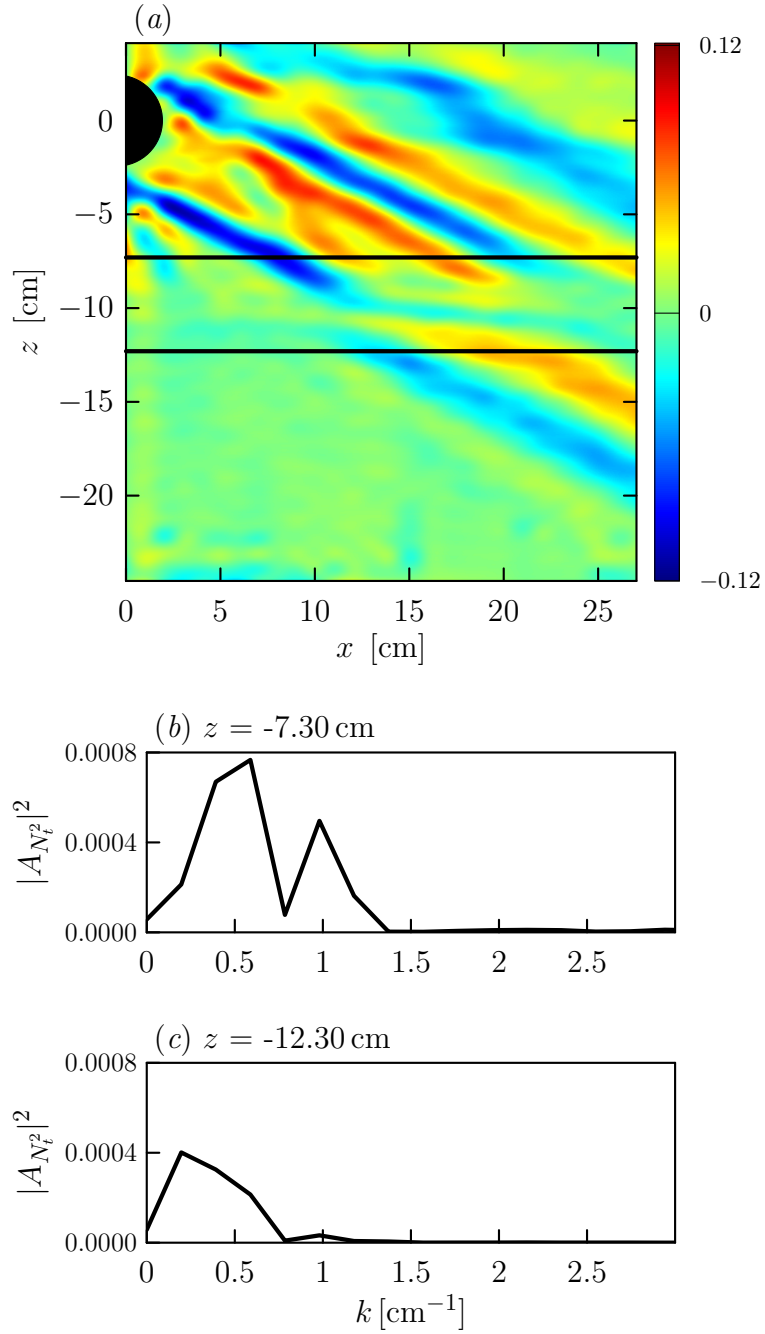


Figure 4.3: (a) A Hilbert filtered snapshot of a beam generated by an oscillating cylinder, tunnelling through a weakly stratified region. (b) The Fourier transform of a horizontal slice taken above the weakly stratified region, and (c) the Fourier transform of a horizontal slice taken below the weakly stratified region.

Table 4.1: Table of parameters and errors for oscillating cylinder experiments. Typical errors are indicated in the first row except for the value of N_1 which underestimates N_{thy} as indicated.

Exp	ω_c [s^{-1}]	N_0 [s^{-1}]	N_1 [s^{-1}]	σ [cm]	L [cm]
1b	0.50 ± 0.01	1.11 ± 0.01	$0.43 + 0.06$	0.90 ± 0.05	3.20 ± 0.05
1c	0.50	1.16	$0.46 + 0.01$	1.00	5.95
1d	0.50	1.20	$0.34 + 0.01$	1.35	7.75
2b	0.51	1.40	$0.42 + 0.07$	0.80	3.25
2c	0.51	1.40	$0.33 + 0.09$	0.75	3.15
2d	0.51	1.51	$0.00 + 0.31$	1.65	6.30
2e	0.51	1.55	$0.06 + 0.14$	1.75	8.45
3b	0.47	1.38	$0.27 + 0.20$	1.10	3.50
3c	0.47	1.41	$0.18 + 0.14$	1.55	6.20
3d	0.47	1.48	$0.00 + 0.31$	1.55	8.15
4b	0.52	1.43	$0.40 + 0.13$	1.40	4.75
4c	0.52	1.52	$0.36 + 0.05$	1.60	7.55
4d	0.51	1.60	$0.00 + 0.19$	1.80	8.95
5b	0.52	1.48	$0.52 + 0.06$	1.30	5.20
5c	0.52	1.53	$0.27 + 0.10$	1.60	6.95
5d	0.52	1.60	$0.18 + 0.10$	2.00	9.30
6b	0.52	1.43	$0.26 + 0.28$	1.35	3.80
6c	0.52	1.52	$0.45 + 0.06$	1.80	7.55
6d	0.52	1.57	$0.14 + 0.08$	1.65	8.48

Table 4.2: Table of nondimensional parameters and theoretical and experimental transmission coefficients for oscillating cylinder experiments.

Exp	N_1/N_0	σ/L	$k_c L$	ω_c/N_0	ω_c/N_1	T_{exp}	T_{thy}
1b	0.38	0.28	0.93	0.45	1.17	0.68	0.52
1c	0.40	0.17	1.66	0.43	1.08	0.28	0.27
1d	0.28	0.17	2.08	0.42	1.49	0.14	0.08
2b	0.30	0.25	0.77	0.36	1.21	0.36	0.53
2c	0.24	0.24	0.74	0.36	1.52	0.39	0.51
2d	0	0.26	1.38	0.34	$\rightarrow \infty$	0.18	0.23
2e	0.04	0.21	1.80	0.33	8.27	0.07	0.09
3b	0.20	0.31	1.88	0.34	1.73	0.09	0.49
3c	0.13	0.25	3.24	0.33	2.64	0.04	0.16
3d	0	0.19	4.08	0.32	$\rightarrow \infty$	0.04	0.06
4b	0.28	0.29	2.71	0.36	1.30	0.21	0.47
4c	0.23	0.21	4.05	0.34	1.46	0.07	0.11
4d	0	0.20	4.47	0.32	$\rightarrow \infty$	0.02	0.02
5b	0.35	0.25	2.86	0.35	1.00	0.22	0.62
5c	0.18	0.23	3.71	0.34	1.92	0.11	0.08
5d	0.11	0.22	4.74	0.32	2.88	0.04	0.04
6b	0.18	0.36	2.17	0.36	2.02	0.18	0.55
6c	0.29	0.24	4.07	0.34	1.17	0.06	0.38
6d	0.09	0.19	4.40	0.33	3.77	0.03	0.02

4.3 Transmissions for rotating disk experiments

A similar processing method was used for experiments performed with the rotating disks. We will briefly review this in the context of a particular experiment for which the rotating disks create a horizontal displacement oscillation amplitude of 0.33 cm and rotate with frequency $\omega_c = 0.91 \text{ s}^{-1}$. A single density profile taken before running the experiment was empirically fit to the smooth analytic curve (3.3) and the optimal parameters were found to be $N_0 = 1.43 \text{ s}^{-1}$, $N_1 = 1.02 \text{ s}^{-1}$, $z_u = -6.85 \text{ cm}$, $z_l = -20.55 \text{ cm}$, $\sigma_u = \sigma_l = 1.50 \text{ cm}$ and $\rho_0 = 1.01 \text{ g/cm}^3$. The fit to the background density fit and the corresponding N^2 profile are shown in Figure 4.4. In this case $\omega_c^2 \gtrsim N_1^2$.

The synthetic schlieren process was used to produce snapshots of the N_t^2 field. A snapshot at 10 buoyancy periods (time = 69 s) is shown in Figure 4.5(b), along with a sample vertical time series in Figure 4.5(a). The Hilbert transform is applied to filter out waves reflecting off the mixed region, as shown in Figure 4.5(c,d).

As before, amplitudes and horizontal wavenumbers for plane wave components of the wavepacket were obtained by taking horizontal slices of the steady state N_t^2 snapshot above and below the mixed region. The upper slice is taken at $z_u + \sigma_u = -6.85 \text{ cm} + 1.50 \text{ cm} = -5.35 \text{ cm}$, and the lower slice is taken at $z_l - \sigma_l = -20.55 \text{ cm} - 1.50 \text{ cm} = -22.05 \text{ cm}$, where $z = 0$ now corresponds to the bottom of the rotating disks. Plane wave amplitudes and horizontal wavenumbers found by taking a Fourier transform in the x -direction of both slices are shown in Figure 4.6(b,c).

In these experiments we found the incident beam to be less quasi-monochromatic, exciting more than one significant peak in $|A_{N_t^2}(k_n)|^2$. This was attributed to turbulent mixing near the disks, which provided an alternate source for wave excitation. The experimental and theoretical transmission

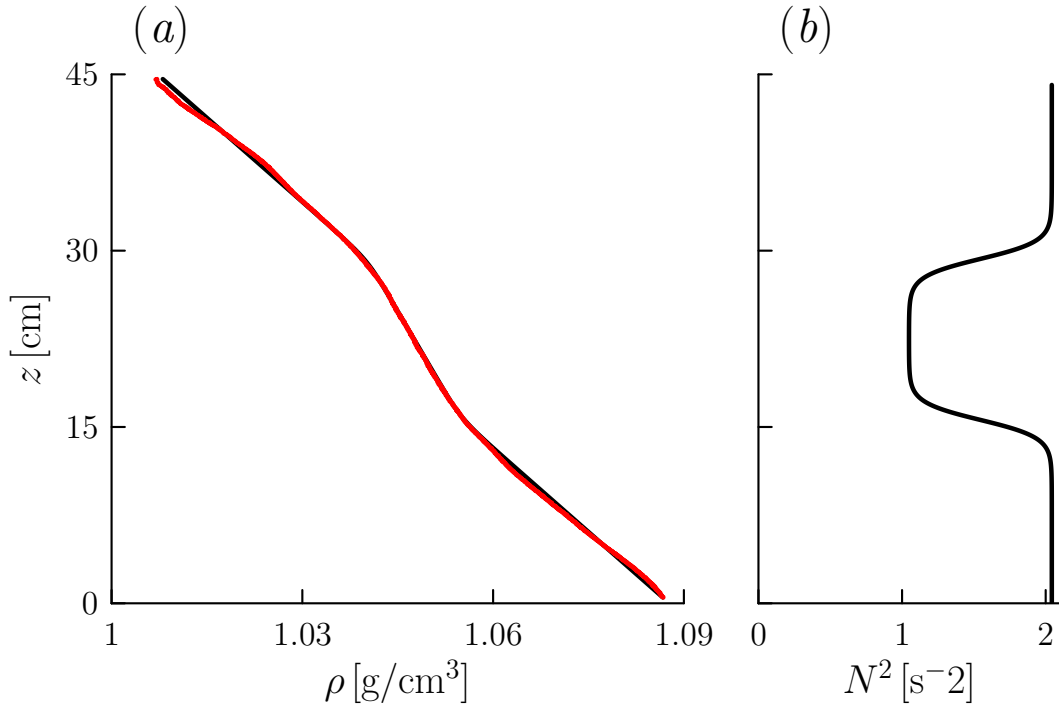


Figure 4.4: Background profiles for a rotating disk experiment. (a) The red curve is the experimental background density profile and the black curve is its smooth analytic fit. (b) The background N^2 profile based on the parameters found for the smooth analytic density profile fit.

coefficients for the beam were calculated in exactly the same way as with the oscillating cylinder case. The parameters used in the rotating disk experiments are recorded in Table 4.3 and their experimental and theoretical transmission coefficients are compared in Table 4.4. The particular experiment shown in Figure 4.5 is denoted “7b”.

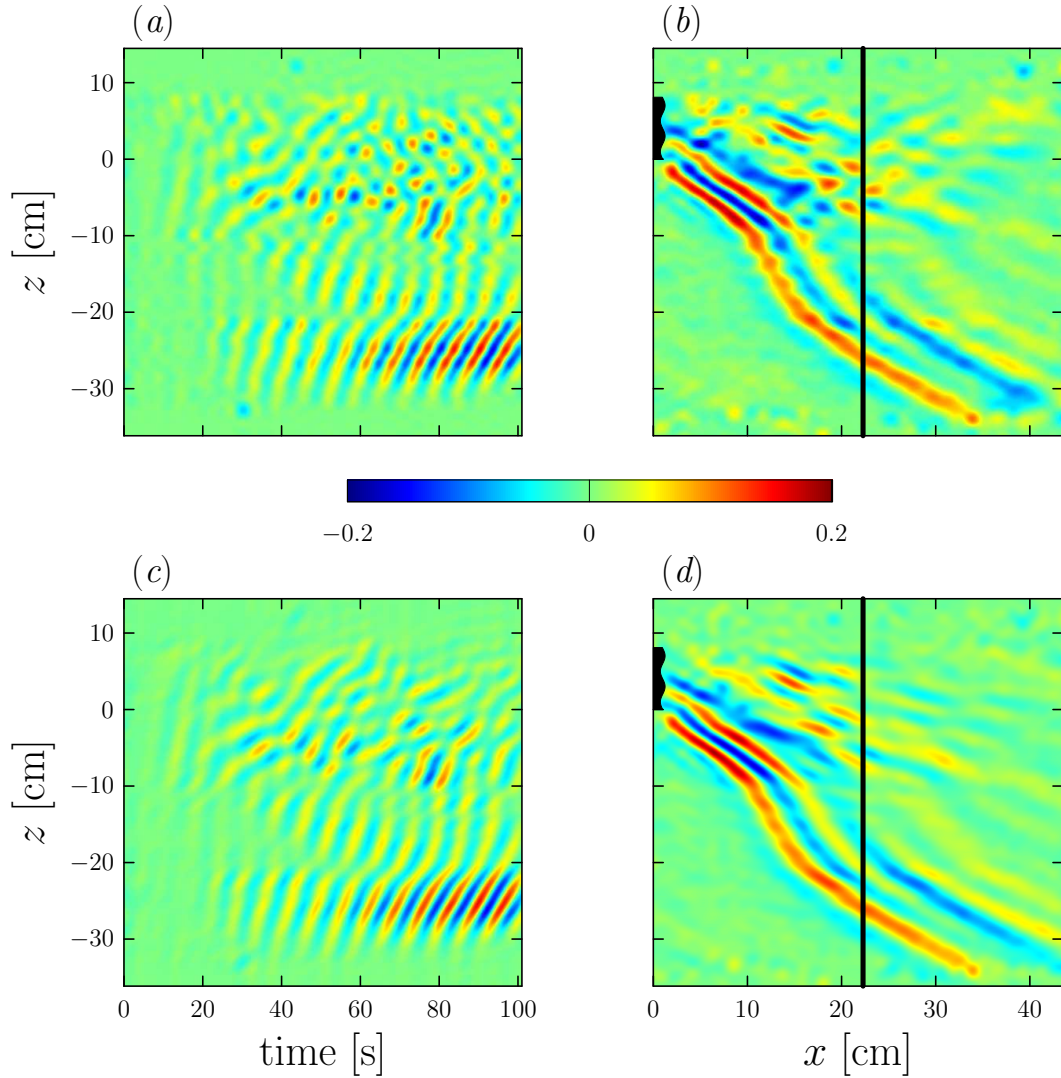


Figure 4.5: A vertical time series taken at $x = 22.28$ cm from the bottom of the disks is shown in (a). 42 of these vertical time series are used to reconstruct a snapshot of the N_t^2 field, (b), at time=69s. Using the Hilbert transform to filter out $m < 0$ from each vertical time series, (c), a clean view of the downward travelling beam can be seen in (d). All plots are smoothed for ease of viewing.

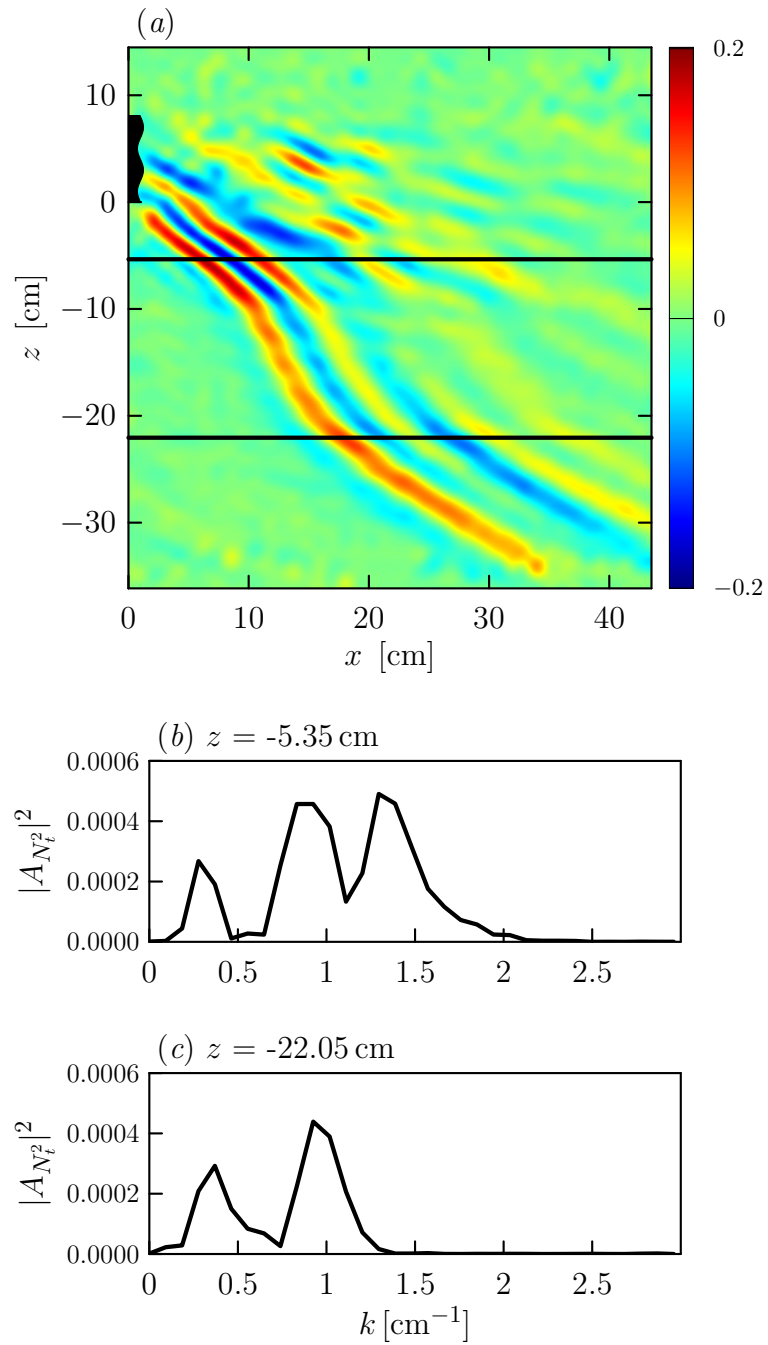


Figure 4.6: (a) A Hilbert filtered snapshot of a beam generated by the rotating disks, tunnelling through a weakly stratified region. (b) The Fourier transform of a horizontal slice taken above the weakly stratified region, and (c) the Fourier transform of a horizontal slice taken below the weakly stratified region.

Table 4.3: Table of parameters and errors for rotating disk experiments. Typical errors are indicated in the first rows except for the value of N_1 which underestimates N_{thy} as indicated.

Exp	ω_c [s ⁻¹]	N_0 [s ⁻¹]	N_1 [s ⁻¹]	σ [cm]	L [cm]
7b	0.91 ± 0.01	1.43 ± 0.01	$1.02 + 0.00$	1.50 ± 0.05	13.70 ± 0.05
7c	0.91	1.50	$0.80 + 0.01$	2.70	16.60

Table 4.4: Table of nondimensional parameters and theoretical and experimental transmission coefficients for rotating disk experiments.

Exp	N_1/N_0	σ/L	$k_c L$	ω_c/N_0	ω_c/N_1	T_{exp}	T_{thy}
7b	0.72	0.11	17.77	0.64	0.89	0.77	0.89
7c	0.54	0.16	19.96	0.61	1.13	0.08	0.04

4.4 Discussion of results

Considering any of the sets of experiments where successive intrusions are released, the trend shows that as the depth of the mixed region, L , increases, the transmission coefficient decreases. Since the waves generated after each intrusion have the same frequency, ω_c , and horizontal wavenumber, $k_c \equiv \frac{\pi}{2R} \cos \Theta$, then the parameter $k_c L$ will always increase. This is consistent with the results shown in Section 2.5 where transmission decreased as $k_c L$ increased for a fixed wave frequency.

The sensitivity analysis of σ/L conducted in Chapter 3 found an upper limit of $\sigma/L = 0.2$ for accurately fitting N_1 . From Tables 4.2 and 4.4, most of the values of σ/L are at or above this limit suggesting that the measured experimental N_1 values will not be attained accurately using the smooth analytic

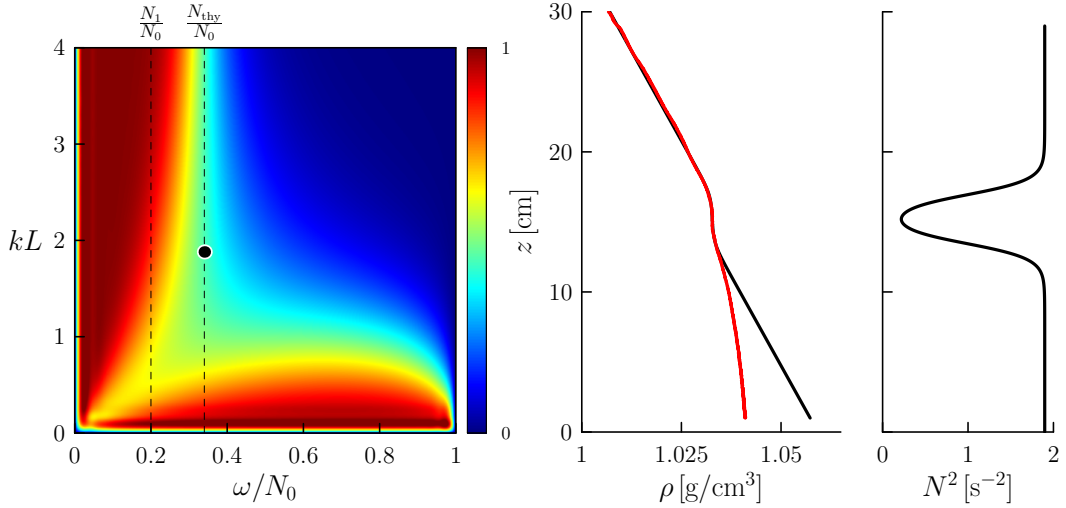


Figure 4.7: Theoretical transmission coefficient plot for experiment 3b. The black circle on the transmission plot indicates the theoretical transmission coefficient for this experiment, where $\omega = \omega_c$ and $k = k_c$. Vertical dashed lines indicate values where $\omega = N_1$ and $\omega = N_{\text{thy}}$. To the right are background profiles of density and squared buoyancy frequency where the red line is the experimental data and the black lines are the smooth analytic profiles using the fitted parameters. Note, the experimental probe data are unreliable below $z \approx 12$ cm due to failure of the conductivity probe electronics for very strong saline solutions.

N^2 formula. The few experiments which have σ/L below this limit, namely 1c, 1d, 3d, 6d, 7b and 7c, have experimental and theoretical transmissions that generally agree.

Some of the transmission results shown in Tables 4.2 and 4.4 reveal significant discrepancies in the comparison of experiments and theory. We will discuss the general trends in the data and focus on three specific experiments to help explain the origin of the discrepancies.

Consider experiment 3b, in which the experimental transmission is much smaller than the theoretical transmission. For this experiment, $\omega_c = 0.47 \text{ s}^{-1}$, $N_0 = 1.38 \text{ s}^{-1}$, $k_c \approx 0.54 \text{ cm}^{-1}$ and $L = 3.50 \text{ cm}$. The measured experimental value of N_1 is 0.27 s^{-1} while its attained value using the analytic formula, N_{thy} , is 0.47 s^{-1} , making a difference of 0.20 s^{-1} . Recall from Section 2.5 that for moderately large $k_c L$ the transmission varies rapidly with ω/N_0 when

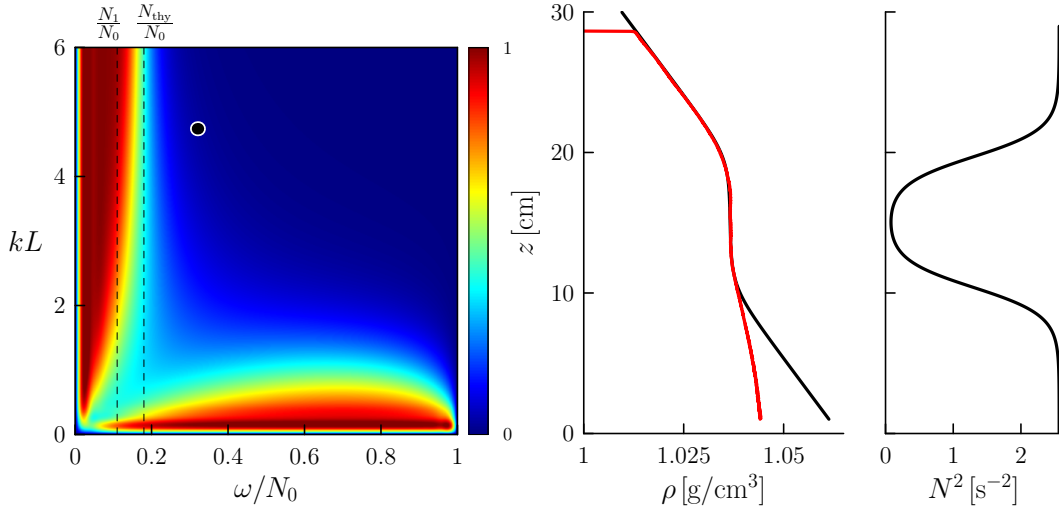


Figure 4.8: As in Figure 4.7 except showing the theoretical transmission coefficient plot and density and N^2 profiles for experiment 5d.

ω_c is close to N_1 , the transition region. This is shown in Figure 4.7, which plots the theoretical transmission coefficients for a range of ω and k for this experiment. The theoretical transmission coefficient, $T_{\text{thy}} = 0.49$, occurs at $\omega_c/N_0 = 0.34$ and $k_c L \approx 1.88$, as indicated in Figure 4.7. Because the wave frequency occurs within the transition region where $N_1 \lesssim \omega_c \lesssim N_{\text{thy}}$ and because $N_1/N_0 = 0.20$ is significantly less than $N_{\text{thy}}/N_0 = 0.34$, the error in predicted transmission is large. T_{thy} was computed from analytic curves for which the minimum buoyancy frequency was N_{thy} . But direct measurements show that the minimum, N_1 , is smaller, hence the actual waves pass through a more weakly stratified region and are more strongly evanescent. Thus the measured transmission coefficient, $T_{\text{exp}} = 0.09$, is significantly smaller than the theoretical transmission coefficient.

The second experiment we consider is denoted 5d, whose experimental and theoretical transmissions are relatively low and in good agreement. For this experiment, $\omega_c = 0.52 \text{ s}^{-1}$, $N_0 = 1.60 \text{ s}^{-1}$, $k_c \approx 0.51 \text{ cm}^{-1}$ and $L = 9.30 \text{ cm}$. The measured experimental value of N_1 is 0.18 s^{-1} while its attained value using the analytic formula, N_{thy} , is 0.28 s^{-1} , making a difference of 0.10 s^{-1} .

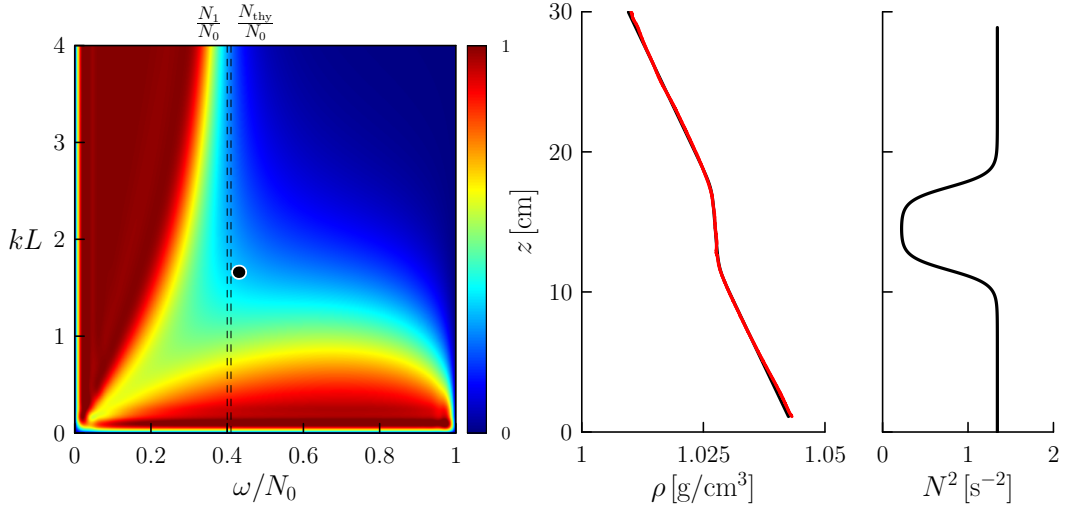


Figure 4.9: As in Figure 4.7 except showing the theoretical transmission coefficient plot and density and N^2 profiles for experiment 1c.

Figure 4.8 shows a plot of theoretical transmission coefficients for a range of ω and k for this experiment. The theoretical transmission coefficient, $T_{\text{thy}} = 0.04$, occurs for $\omega_c \gg N_1, N_{\text{thy}}$, which is well away from the transition region. Thus we expect little difference between the experimental transmission coefficient, $T_{\text{exp}} = 0.04$, and the theoretical transmission coefficient.

The third experiment we consider is denoted 1c, whose experimental and theoretical transmissions are relatively high and in good agreement. For this experiment, $\omega_c = 0.50 \text{ s}^{-1}$, $N_0 = 1.16 \text{ s}^{-1}$, $k_c \approx 0.28 \text{ cm}^{-1}$ and $L = 5.95 \text{ cm}$. The measured experimental value of N_1 is 0.46 s^{-1} while its attained value using the analytic formula, N_{thy} , is 0.47 s^{-1} , making a difference of 0.01 s^{-1} . Figure 4.9 shows a plot of theoretical transmission coefficients for a range of ω and k for this experiment. The theoretical transmission coefficient, $T_{\text{thy}} = 0.27$, occurs for $N_1 \lesssim \omega_c \lesssim N_{\text{thy}}$ which is on the outer right edge of the transition region. However, since $N_1/N_0 \approx N_{\text{thy}}/N_0$, the error in predicted transmission is small. Thus we expect little difference between the experimental transmission, $T_{\text{exp}} = 0.28$, and the theoretical transmission coefficient.

Chapter 5

Conclusions

Internal wave tunnelling through mixed and weakly stratified regions was studied through the analysis of laboratory data. Most experiments were done with a vertically oscillating cylinder producing a cross-pattern of wave beams. Several techniques were applied in order to acquire the clearest images of the primary beam. Among these was the use of the Hilbert transform which removed the part of the wave beam that reflected off the weakly stratified region. Additional laboratory experiments were also performed using a rotating stack of disks formed into a helical shape so as to produce only the single primary wave beam. Experimental transmission coefficients were measured explicitly by finding the amplitudes of the plane waves of the beam above and below the mixed region. Theoretical transmission coefficients were computed using a numerical code that integrated the Taylor-Goldstein equation to find transmission coefficients for plane waves. This code required a smooth continuous background squared buoyancy frequency profile. To satisfy these conditions, a smooth analytic function was fit to the experimental profiles.

After comparing the theoretical transmissions to the experimental transmissions, we determined that even with attempts being made to produce a clean beam signal in some experiments there was poor agreement between the predicted and measured transmissions.

Specifically addressed in this study were the effects of σ/L on the stratification of the weakly stratified region, N_{thy} , used for the theoretical calculations. This differed significantly from the measured minimum value, N_1 , if $\sigma/L \gtrsim 0.2$. It was found that if $N_1 \simeq N_{\text{thy}}$ then there was good agreement between the experimental and theoretical transmission coefficients, regardless of the frequency of the waves, ω_c . However, if N_{thy} was significantly larger than N_1 and $N_1 \lesssim \omega_c \lesssim N_{\text{thy}}$, then agreement between transmission coefficients was poor. Agreement was good if ω_c was much smaller or larger than the values of N_1 and N_{thy} .

Based on our experiments, we found that internal wave transmission between regions of strong stratification separated by weak stratification is very sensitive to the buoyancy frequency of the weak stratification region as well as if the wave's frequency is close to this minimum buoyancy frequency. In the atmosphere, internal waves are known to tunnel between the stratosphere and the ionosphere by way of the weakly stratified mesosphere (Yamada et al., 2001; Walterscheid et al., 2001; Snively and Pasko, 2003). Our study shows that for accurate transmission predictions measurements of the buoyancy frequency profile taken in the mesosphere would need to be accurate for incident upward-propagating waves with frequency close to the minimum buoyancy frequency of the mesosphere. The same is true for tunnelling in the ocean where internal waves pass between the strongly stratified seasonal and main thermoclines: the ability to predict accurately the amount of energy transported by incident downward-propagating waves would be poor if the wave frequency was comparable to the minimum buoyancy frequency between the thermoclines. Because measurements are taken infrequently in these regions, predictions of energy transfer due to internal wave tunnelling are not likely to be accurate in such circumstances.

Bibliography

- Bretherton, F. P. (1966). Propagation of groups of internal gravity waves in shear flow. *Quart. J. Roy. Meteorol. Soc.* *92*, 466–480.
- Broutman, D., J. W. Rottman, and S. D. Eckermann (2004). Ray methods for internal waves in the atmosphere. *Annu. Rev. Fluid Mech.* *36*, 233–253.
- Brown, G. L. and B. R. Sutherland (2007). Internal wave tunnelling through non-uniformly stratified shear flow. *Atmosphere-Ocean* *45* (1), 47–56.
- Croquette, V. and H. Williams (1989). Nonlinear waves of the oscillatory instability on finite convective rolls. *Physica D* *37*, 300–314.
- Dalziel, S. B., G. O. Hughes, and B. R. Sutherland (2000). Whole field density measurements. *Expt. Fluids* *28*, 322–335.
- Drazin, P. G. and W. H. Reid (1981). *Hydrodynamic Stability*. Cambridge University Press.
- Eckart, C. (1961). Internal waves in the ocean. *Phys. Fluids* *4*, 791–799.
- Fritts, D. C. and L. Yuan (1989). An analysis of gravity wave ducting in the atmosphere: Eckart’s resonances in thermal and Doppler ducts. *J. Geophys. Res.* *94* (D15), 18455–18466.
- Garnier, N. B., A. Chiffaudel, F. Daviaud, and A. Prigent (2003). Nonlinear dynamics of waves and modulated waves in 1d thermocapillary flows. I. General presentation and periodic solutions. *Physica D* *174*, 1–29.

- Gostiaux, L., H. Didelle, S. Mercier, and T. Dauxois (2007). A novel internal waves generator. *Exps. Fluids* 42, 123–130. doi:10.1007/s00348-006-0225-7.
- Hurley, D. G. and G. Keady (1997). The generation of internal waves by vibrating elliptic cylinders. Part 2. Approximate viscous solution. *J. Fluid Mech.* 351, 119–138.
- Lighthill, M. J. (1978). *Waves in Fluids*. Cambridge University Press.
- Mercier, M. J., N. B. Garnier, and T. Dauxois (2008). Reflection and diffraction of internal waves analyzed with the hilbert transform. *Physics of Fluids* 20. doi:10.1063/1.2963136.
- Mowbray, D. E. and B. S. H. Rarity (1967). A theoretical and experimental investigation of the phase configuration of internal waves of small amplitude in a density stratified liquid. *J. Fluid Mech.* 28, 1–16.
- Nault, J. T. and B. R. Sutherland (2007). Internal wave transmission in non-uniform flows. *Phys. Fluids* 19.
- Oster, G. (1965). Density gradients. *Scientific American* 213, 70.
- Snively, J. B. and V. P. Pasko (2003). Breaking of thunderstorm-generated gravity waves as a source of short-period ducted waves at mesopause altitudes. *Geophys. Res. Lett.* 30(24), 2254.
- Sutherland, B. R. (2002). Large-amplitude internal wave generation in the lee of step-shaped topography. *Geophys. Res. Lett.* 29(16). doi:10.1029/2002GL015321.
- Sutherland, B. R. and K. Yewchuk (2004). Internal wave tunnelling. *J. Fluid Mech.* 511, 125–134.

Walterscheid, R. L., G. Schubert, and D. G. Brinkman (2001). Small-scale gravity waves in the upper mesosphere and lower thermosphere generated by deep tropical convection. *J. Geophys. Res.* *106*(D23), 21825–31832.

Yamada, Y., H. Fukunishi, T. Nakamura, and T. Tsuda (2001). Breaking of small-scale gravity waves and transition to turbulence observed in OH airglow. *28*(11), 2153–2156.